This article has been accepted for publication in IEEE Transactions on Vehicular Technology. This is the author's version which has not been fully edited and content may change prior to final publication. Citation information: DOI 10.1109/TVT.2021.3102315

Reconfigurable Intelligent Surfaces for N-LOS Radar Surveillance

Augusto Aubry, *Senior Member, IEEE*, Antonio De Maio, *Fellow, IEEE*, and Massimo Rosamilia, *Student Member, IEEE*

***Abstract*—This paper deals with the use of Reconfigurable Intelligent Surfaces (RISs) for radar surveillance in Non-Line Of Sight (N-LOS) scenarios. First of all, the geometry of the scene and the new system concept is described with emphasis on the required operative modes and the role played by the RIS. Then, the specific radar equation (including the RIS effect) is developed to manage the coverage requirements in the challenging region where the LOS is not present. Both noise and clutter interference cases (pulse length-limited and beamwidth-limited surface clutter as well as volume clutter) are considered. Hence, a digression on the use of the radar timeline for the new operative mode is presented together with the data acquisition procedure and the resolution issues for the range, azimuth, and Doppler domains. Finally, the interplay among the system parameters and, in particular, those involving the RIS is discussed and analyzed via numerical simulations.**

***Index Terms*—Reconfigurable Intelligent Surfaces, Around the Corner Radar, Radar Equation with RIS.**

I. Introduction

Reconfigurable Intelligent Surfaces (RISs) (also known in the open literature as intelligent reflecting surfaces, smart reflectarrays, large intelligent surfaces, metasurfaces, and so on) are a novel and promising technology which is receiving growing interest in recent years especially for next generation communication (e.g., beyond 5G and future 6G) and sensing systems [1]–[13]. RISs are man-made digitally controllable meta-surfaces [14], composed of a very large number [15] of low-cost passive programmable integrated electronic circuits, capable of varying the electric field distribution of the impinging signals, i.e., phase, amplitude, frequency, and polarization features, via appropriate electronic controls [16]. Therefore, they pave the way to the "lifelong dream" of eliminating the Radio Frequency (RF) propagation medium randomness and avoiding the resulting deleterious effects, by means of a wisely designed electromagnetic waves interaction. Otherwise stated, they lay the ground to the paradigm of *smart radio environments* [17].

The use of RIS was firstly proposed for communication purposes in [18], but it has gained serious attention from the research community since its employment as a phase-shifter in [19]. Nowadays, excellent tutorial papers are available in open literature about diverse aspects connected with RIS technology and usage. For instance, hardware issues are addressed in [17] and [20]; applications for communication purposes are addressed in [3], [21]–[25]; localization aspects are considered in [26]–[31] whereas a signal processing perspective is provided in [32]. They also contain a selection of references which extensively span the state of the art for the current literature.

As to the radar research field, applications of the RIS concept are mainly related to the use of meta-surfaces for target Radar Cross Section (RCS) reduction [33], [34]. Recently, other specific radar signal problems have also been tackled via RIS. Precisely, in [10] the RIS is integrated in a Dual-function Radar and Communication (DRC) system to improve radar detection performance in a crowded area with severe path loss. In [7] and [9], the RIS is employed for colocated Multiple-Input Multiple-Output MIMO and Distributed MIMO (DMIMO) radar systems, respectively. The last reference capitalizes the presence of the intelligent surface which, via a specific coordination, aims at increasing the signal power from the prospective target. Additional technically sound strategies for RIS-aided MIMO radars are available in [35], [36].

At large the new technology appears promising to aid a multitude of radar applications. Leveraging this last observation, the present paper is aimed at exploring the usage of RIS for radar detection in the absence of a direct path between radar and target. This is of primary interest in many practical civilian and military scenarios. In fact, the so called "around-the-corner radar" (see [37]–[40] and references therein) can be regarded as a present-day and very challenging issue for security concerns especially in urban environments which are densely populated by small moving targets such as pedestrians and small Unmanned Aerial Vehicles (UAV). It is quite common that such kind of targets might fall in a shadow area (caused for instance by a tall building) blocking the LOS. As a consequence, the signal and data processing require adaptation to this unconventional propagation situation and new techniques are demanded to handle the problem. The major strategies developed in the open literature rely on natural multipath capitalization and/or on the use of radar networks. For instance, in [40] detection and localization of targets in Non-Line Of Sight (N-LOS) areas with a single portable radar via multipath exploitation is addressed. Two algorithms (which process the multipath returns) are proposed to detect the target and estimate its N-LOS position. In [41], a system incorporating distinct radar sensors (with communication capabilities)

The work of A. Aubry and A. De Maio was partially funded by research program ARS01 00615 (University of Naples Federico II).

Augusto Aubry, Antonio De Maio (Corresponding Author), and Massimo Rosamilia are with the Department of Electrical Engineering and Information Technology, Università degli Studi di Napoli "Federico II", DIETI, Via Claudio 21, I-80125 Napoli, Italy, and also affiliated with CNIT, Italy, E-mail: augusto.aubry@unina.it, ademaio@unina.it, massimo.rosamilia@unina.it.

is developed for UAV detection in a urban environment. It includes small radar sensor nodes (with a limited detection range) aimed at ground/sky surveillance or at street search across two opposite walls. Besides, in the scenario addressed in [41], a standard rotating radar (based on LOS) covering the flight space completes the network. A network of low-cost Commercial-Off-The-Shelf (COTS) radars, mounted on the facades of buildings or the street lamp sites, is designed in [42] to detect small drones and establish a continuous coverage in urban environment.

A different perspective is provided in the present study where RIS technology is proposed to extend the coverage of a standard radar system whereby the direct LOS from a prospective target is missing. The basic idea is to place one or more RISs in suitable positions (fixed or possibly deployable on request together with a portable radar) within the operating environment such that there is always a direct path between the radar and each RIS. Besides, in each shadow region (where the direct radar-target path is absent), there is at least a RIS with a LOS toward the target. Thus, the region under test is scanned according to two different radar operative modes. The former is for the search in areas with a direct path radar-target and is nothing more than a classic radar modality. The latter, designed for operation in N-LOS areas, is based on the formation of a smart and controlled propagation environment where the radar focuses the radiation on a specific RIS. The RIS parameters are suitably set to perform scanning within its area of competence. Hence, after target backscattering and another programmed reflection of the RIS to the radar, a two-way double-hop channel is established which allows to accomplish the surveillance task. Alternation between the operative modes ensures the coverage of the entire region of interest.

For the new N-LOS modality, the radar equation for the Signal to Noise Ratio (SNR) budget [43], [44], [45, ch. 2], is derived including the RIS effects as well as the presence of the two hops in the forward and reverse link. Moreover, the Signal to Clutter Ratio (SCR) is computed accounting for either surface or volume clutter. A discussion on resolution parameters connected with the new mode is provided together with the procedure for data acquisition and formation of the fast-time slow-time data matrix. Remarkably, after this step, classic and consolidated range-Doppler processing, possibly leveraging clutter cancellation procedures and Constant False Alarm Rate (CFAR) techniques, can be used. At the analysis stage the SNR and the detection Probability (P_d) are evaluated to assess the performance of the N-LOS mode and to highlight the role of the system parameters with special emphasis on those characterizing the RIS.

Summarizing, the main contributions of this paper are:

1) to the best of authors' knowledge, this is the first attempt to addresses the problem of radar detection and localization in N-LOS conditions with the aid of a RIS.
2) the derivation of the radar equation for the SNR assessment in RIS-aided surveillance system in N-LOS mode;
3) the computation of the SCR accounting for either surface or volume clutter in N-LOS links via RIS;
4) a discussion on resolution parameters connected with the new sensing mode together with the procedure for data acquisition and fast-time slow-time data matrix formation;
5) a numerical analysis, in terms of SNR and P_d, is provided to assess the effectiveness of the proposed solution to N-LOS surveillance, shedding light on the impact of the system parameters with special emphasis on those characterizing the RIS.

The paper is organized as follows. Section II presents a brief introduction to RIS technology and introduces the RIS-assisted system for radar surveillance in N-LOS environments. In Section III, the radar equation is reformulated to account for the RIS presence in the computation of the SNR. The expressions of the SCR are derived in Section IV. Section V discusses the use of the radar timeline, data acquisition, and resolution issues for the N-LOS mode, whereas numerical results are presented in Section VI. Finally, Section VII draws some conclusions and highlights possible future research avenues.

A. Notation

Boldface is used for vectors $\boldsymbol{a}$ (lower case), and matrices $\boldsymbol{A}$ (upper case). The all-ones column vector of size N is indicated as $\mathbf{1}_N$. The transpose and the conjugate operators are denoted by the symbols $(\cdot)^{\mathrm{T}}$ and $(\cdot)^*$, respectively. Besides, the Hadamard (i.e., elementwise) product is indicated as $\odot$. The set of N-dimensional column vectors of complex numbers is represented by $\mathbb{C}^N$ whereas $\mathbb{C}^{N,M}$ denotes the set of $N \times M$-dimensional matrices of complex numbers. The letter j indicates the imaginary unit (i.e., $j = \sqrt{-1}$). For any complex number x, $|x|$ indicates the modulus of x. Furthermore, for any $x, y \in \mathbb{R}$, $\max(x, y)$ returns the maximum between the two argument values. Finally, for any $\boldsymbol{x} \in \mathbb{C}^N$, $\|\boldsymbol{x}\|$ denotes the Euclidean norm.

II. A Brief Introduction to RIS Technology and Working Principles for its Application to N-LOS Radar Operation

Before investigating the exploitation of metasurfaces for radar surveillance without LOS, a brief introduction of RIS technology is now provided.

Characterized by single or multi-layer (typically three) planar structures employing Micro Electro-Mechanical Systems (MEMS) switches, varactor diodes, etc., the RIS can be electronically managed by a general-purpose micro-controller [19] to reflect, refract, or absorb the incident signals with independently controlled amplitude and/or phase shifts [2], [6], [16], [17], [20]–[22], [26], [46]–[48]. These extra degrees-of-freedom can be exploited to enhance the capabilities and the efficiency of a wireless system. In particular, with a proper configuration of the units, the RIS is able to extend the coverage of the transmitter beyond its natural LOS, with an additional path toward the target (virtual LOS link) [21]. Besides, the low profile, regular shape and lightweight makes the RIS suitable for an easy installation in the environment [7], [10], [21], including a deployment into buildings facades, room and factory ceilings, and so on (see also [47]). Two

This article has been accepted for publication in IEEE Transactions on Vehicular Technology. This is the author's version which has not been fully edited and content may change prior to final publication. Citation information: DOI 10.1109/TVT.2021.3102315

recent research prototypes are presented in [49] and [50]; the former is made of inexpensive antennas whereas the latter is a meta-surface. Detailed description of the hardware architectures can be found in [16], [51].

Unlike phased arrays and relays, RISs (being passive or nearly passive [17]) do not require the use of power amplifiers and, even if they demand the largest number of cell elements among the mentioned technologies, they can be realized with the least expensive components [52]. Additional observations about the distinctive peculiarities of RIS, as compared with competing technologies, are discusses in [17].

In the following, a discussion on the use of RISs for radar surveillance without LOS, is provided. The idea is to control artificially the propagation environment to extend the radar coverage in those regions which cannot be reached by the direct path. In this respect, the intelligent surface plays the role of a passive but controllable element of the radar environment which aids the establishment of a radar-target propagation path. An illustration of the basic concept is now provided. The radar is located at point A and has to cover the shaded region (union of sub-region 1 and sub-region 2) displayed in Fig. 1.

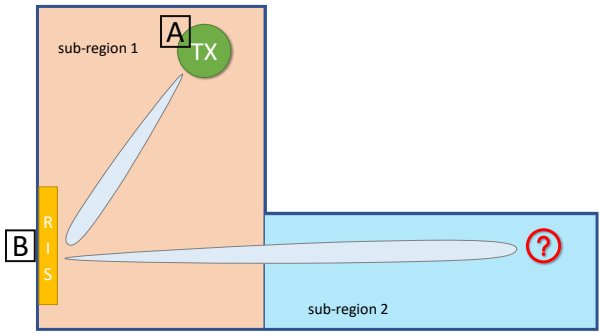

Fig. 1. Geometry of the RIS radar system. The prospective target is located in sub-region 2, which is not directly covered by the radar.

While in sub-region 1 a direct path between the radar and the prospective target can be established, in sub-region 2 a LOS path is no longer present. This situation is representative of a typical radar operation in urban environments or in the presence of natural obstacles (for instance hills, buildings, or natural/artificial wedges) which actually inhibit the direct path. With a standard radar mode a partial coverage of sub-region 2 can be achieved only via natural diffraction or multipath propagation. The approach discussed here (to handle the aforementioned scenarios) relies on the development of innovative radar modes exploiting RISs with the endeavor to build a smart propagation environment capable of ensuring the desired coverage in a controlled way. With reference to the example in Fig. 1 (the concept can be also generalized to include multiple RISs), a suitable radar transmission-reception protocol leveraging the availability of a RIS in position B can be established. Precisely, when the radar performs the standard surveillance operations in sub-region 1, see Fig. 2, the RIS is inactive and classic scanning patterns (i.e., sequential scanning, stacked beams, etc.) can be adopted.

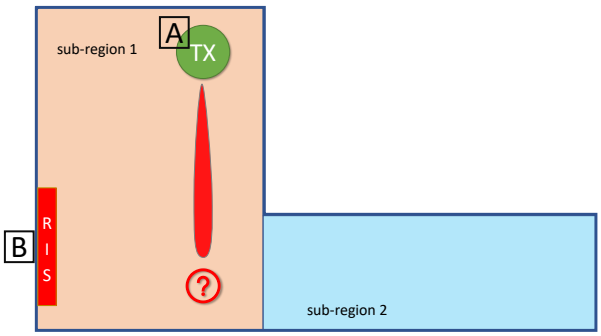

Fig. 2. Geometry of the RIS radar system. The prospective target is directly covered by the radar. The RIS is inactive.

Periodically, according to a desired temporal scheduling, a radar scan in sub-region 2 is demanded. During these time intervals the RIS is turned on and the radar beam is pointed toward the RIS allowing for the angle of the reflected wave to be arbitrarily controlled. This can be done adjusting the RIS characteristic parameters for instance through a pre-canned program or a communication-oriented software which represents another degree of freedom (but also a challenge) in the design of the radar scheduler. Resorting to a specific timing procedure, based on the knowledge of the radar and RIS positions the system can scan through sub-region 2. Just to give an example (even if it is worth mentioning that alternative sweep patterns can be conceived) in Fig. 3, a sequential scanning protocol is displayed where in a specific radar dwell time $T_d = N_p\, T$ (with T the Pulse Repetition Interval (PRI) and N_p the number of transmitted pulses), transmission and reception are alternated. Assuming that H beams are employed to scan the whole sub-region 2, let us focus on the i-th dwell and describe the sequence of involved operations. The radar focuses the beam on the RIS which reflects the radiation to cover the i-th angular sector of sub-region 2. Then the listening time starts where the RIS is programmed to steer the target radiation toward the radar. Hence, the procedure is repeated for the N_p pulses of the dwell. All the signal acquisition as well as signal and data processing is performed at the radar side also accounting for the extra-path (two-way) between the radar and RIS. Then, the scanning of sub-region 2 continues in order to cover the entire area of interest according to different beams (see beams 1, ..., H in Fig. 3).

III. Radar Equation for Sub-region 2

While the standard radar equation [45] can be used to describe the coverage in sub-region 1, a suitable reformulation is necessary for the operation in sub-region 2, to explicitly account for the effects of the RIS and obtain a design tool for system sizing.

In the following it is supposed that the RIS is in the far-field region of both the radar and the target. To proceed further, let us denote by $\boldsymbol{s}_R$, $\boldsymbol{s}_{RIS}$, and $\boldsymbol{s}_T$ the phase-center position of the radar antenna, the RIS, and the target respectively, see Fig. 4. Therein, two Cartesian Reference Systems (CRSs), referred to hereafter as CRS_1 and CRS_2, are reported. The former is

This article has been accepted for publication in IEEE Transactions on Vehicular Technology. This is the author's version which has not been fully edited and content may change prior to final publication. Citation information: DOI 10.1109/TVT.2021.3102315

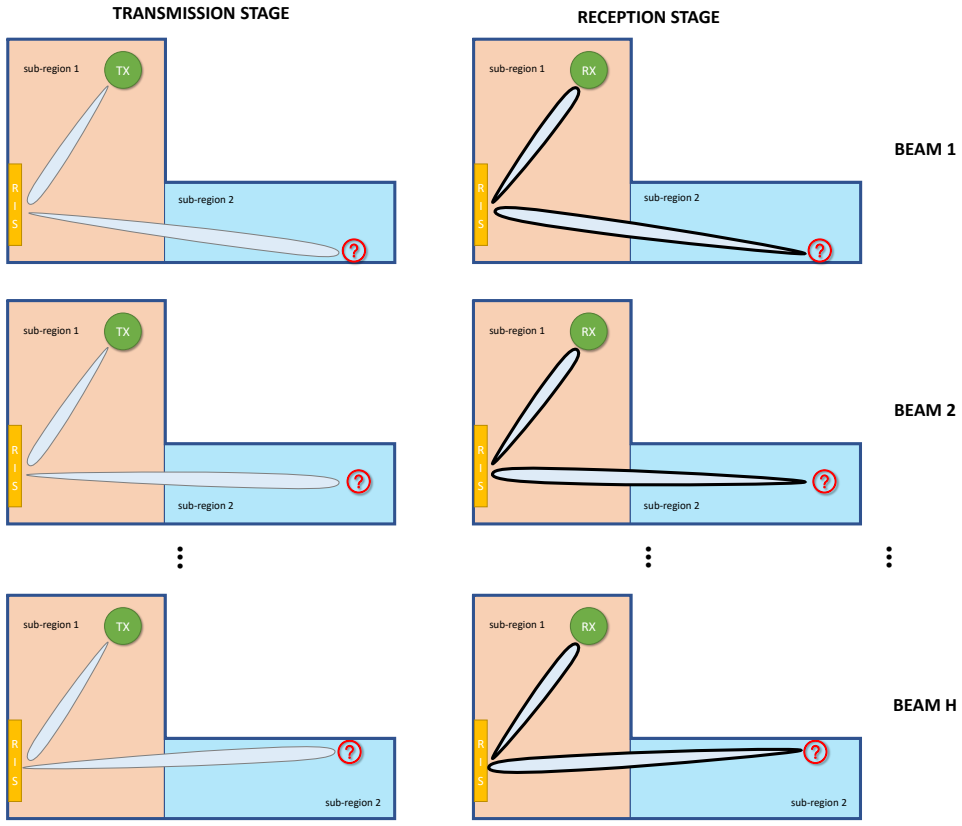

Fig. 3. An example of a sequential scanning of sub-region 2. The left part of the figure reports the transmission stage (TX); the right part refers to the reception stage, with the radar in listening mode (RX). In the i-th dwell, the RIS is properly configured to cover the i-th angular position, $i = 1, \ldots, H$.

centered at $\boldsymbol{s}_R$ and its z-axis coincides with radar antenna pointing direction, the latter is centered at $\boldsymbol{s}_{RIS}$ with the z-axis steered toward the normal to the RIS. Besides, ϕ_R and θ_R refer to the azimuth and elevation angles of the RIS with respect to (w.r.t.) CRS$_1$, respectively, whereas ϕ_{RIS}^R and θ_{RIS}^R indicate the azimuth and elevation angles of the radar w.r.t. CRS$_2$. Furthermore, $\phi_{RIS}^{T_a}$ and $\theta_{RIS}^{T_a}$ represent the azimuth and elevation angles of the target w.r.t. CRS$_2$. Finally, denoting by d_x and d_y the size of each unit patch along the x and y axes[1], respectively, $C_{i,h}$, $i = 1, \ldots, N$, $h = 1, \ldots, M$, indicates the unit cell/patch of the RIS whose center is located, w.r.t. CRS$_2$, at $\boldsymbol{s}_{i,h} = \left[(-\frac{(N-1)}{2} + i - 1)d_x, (-\frac{(M-1)}{2} + h - 1)d_y, 0\right]^T$, where, without loss of generality, it is assumed that both N and M are odd numbers.

Let us now focus on the derivation of the radar-range equation for a RIS-assisted surveillance system and denote by

- P_T the radar peak power;
- G_T the radar transmit antenna gain;
- $r_1 = \|\boldsymbol{s}_R - \boldsymbol{s}_{RIS}\|$ the distance between the radar and the RIS;
- $F^R(\bar{\theta}, \bar{\phi})$ the normalized radar power radiation pattern in the look direction $(\bar{\theta}, \bar{\phi})$ w.r.t. CRS$_1$.

[1]It is worth pointing out that in the following, a perfectly flat RIS is considered. However, the developed signal models and equations can be easily generalized to account for the case of a conformal RIS by leveraging the conformal arrays theory.

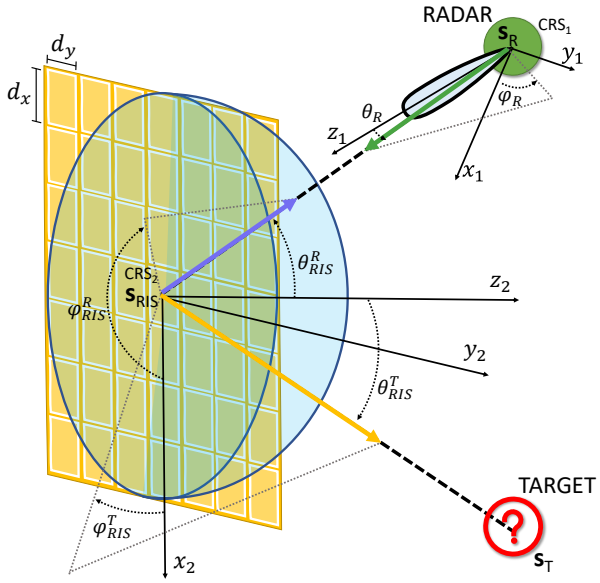

Fig. 4. Model of the RIS-aided sensing system with both the radar and the target assumed located in the far field region of the RIS and vice-versa.

Hence, indicating by $\boldsymbol{E}^{in}$ the matrix collecting in the (i,h)-th entry the electric field (in a given polarization) impinging on the RIS-patch $C_{i,h}$ (due to the radar illumination), it follows,

This article has been accepted for publication in IEEE Transactions on Vehicular Technology. This is the author's version which has not been fully edited and content may change prior to final publication. Citation information: DOI 10.1109/TVT.2021.3102315

under the narrow-band assumption, that

$$\boldsymbol{E}^{in} = \sqrt{2Z_0\mathcal{P}^{in}}\boldsymbol{S}_1 e^{j\phi_1}, \tag{1}$$

where

- $\mathcal{P}^{in} = \frac{G_T P_T F^R(\theta_R,\phi_R)}{4\pi r_1^2}$ is the plane-wave spatial power density at the RIS;
- $\boldsymbol{S}_1 = \boldsymbol{p}_1(\theta^R_{RIS},\phi^R_{RIS})\boldsymbol{p}_2(\theta^R_{RIS},\phi^R_{RIS})^T \in \mathbb{C}^{N,M}$ is the RIS steering matrix associated with radar wave direction of arrival (accounting for the electromagnetic path-lengths between the radar phase-center and the different RIS-patches), with

  $$\boldsymbol{p}_1(\theta_{RIS},\phi_{RIS})=[e^{j\pi\frac{d_x}{\lambda_0}(1-N)u_{RIS}},\ldots,e^{j\pi\frac{d_x}{\lambda_0}(N-1)u_{RIS}}]^T,$$

  $$\boldsymbol{p}_2(\theta_{RIS},\phi_{RIS})=[e^{j\pi\frac{d_y}{\lambda_0}(1-M)v_{RIS}},\ldots,e^{j\pi\frac{d_y}{\lambda_0}(M-1)v_{RIS}}]^T,$$

  the vertical and horizontal RIS manifold vectors, where $u_{RIS} = \sin(\theta_{RIS})\cos(\phi_{RIS})$, $v_{RIS} = \sin(\theta_{RIS})\sin(\phi_{RIS})$ are the directional cosines and λ_0 is the radar operating wavelength;
- Z_0 is the characteristic impedance of the medium;
- ϕ_1 accounts for the phase term related to the propagation path between radar and RIS as well as the phase response of the radar transmit antenna.

Now, denoting by

- $F(\theta,\phi)$ the normalized RIS-patch power radiation pattern at the look direction (θ,ϕ) w.r.t. CRS$_2$,
- η_{RIS} the unit patch efficiency (assumed, for simplicity, common to all the RIS-patches), which accounts for taper and spillover effects [53],

the power gathered by any RIS-patch (due to the radar illumination) is

$$\begin{aligned} P^{RIS} &= \frac{|\boldsymbol{E}^{in}(i,h)|^2}{2Z_0}F(\theta^R_{RIS},\phi^R_{RIS})d_x d_y\eta_{RIS} \\ &= \frac{G_T P_T}{4\pi r_1^2}F^R(\theta_R,\phi_R)F(\theta^R_{RIS},\phi^R_{RIS})d_x d_y\eta_{RIS}, \end{aligned} \tag{2}$$

where $F(\theta^R_{RIS},\phi^R_{RIS})d_x d_y\eta_{RIS}$ is effective antenna area[2] of any RIS-patch [5]. Hence, the electric field *artificially reflected* by $C_{i,h}$ and impinging on the target is given by the (i,h)-th entry of the matrix

$$\boldsymbol{E}^{Target} = \sqrt{\frac{2Z_0 G P^{RIS} F(\theta^{T_a}_{RIS},\phi^{T_a}_{RIS})}{4\pi r_2^2}}\,\boldsymbol{\Sigma}\, e^{j\phi_1}e^{j\phi_2}, \tag{3}$$

where

- $\boldsymbol{\Sigma} = \boldsymbol{S}_1 \odot \boldsymbol{\Gamma} \odot \boldsymbol{S}_2$;
- $\boldsymbol{S}_2 = \boldsymbol{p}_1(\theta^{T_a}_{RIS},\phi^{T_a}_{RIS})\boldsymbol{p}_2(\theta^{T_a}_{RIS},\phi^{T_a}_{RIS})^T$,
- $\boldsymbol{\Gamma} \in \mathbb{C}^{N,M}$ contains at the (i,h)-th entry the programmable reflection coefficients associated with $C_{i,h}$,
- G is the antenna power gain of a RIS-patch;
- $r_2 = \|\boldsymbol{s}_T - \boldsymbol{s}_{RIS}\|$;
- ϕ_2 is the phase term related to r_2.

[2]Additional references concerning effective antenna area concept, also from possible different prospective, are given by [54] and [55].

As a result, the electromagnetic power density impinging on the target is

$$\mathcal{P} = \frac{G_T P_T G F^{tot} d_x d_y \eta_{RIS}}{16\pi^2 r_1^2 r_2^2}|\mathbf{1}_N^T\,\boldsymbol{\Sigma}\,\mathbf{1}_M|^2 \tag{4}$$

with $F^{tot} = F^R(\theta_R,\phi_R)F(\theta^R_{RIS},\phi^R_{RIS})F(\theta^{T_a}_{RIS},\phi^{T_a}_{RIS})$, where to ease the notation the explicit dependence over the angles has been omitted.

Letting σ the monostatic RCS of the target along the LOS with the RIS, the power reflected back by the target toward the RIS is,

$$P_{refl} = \mathcal{P}\sigma. \tag{5}$$

Hence, supposing that the RIS does not change its programmable reflecting coefficients in the backward path and the radar antenna pattern is the same at the transmission and reception stages, i.e., reciprocity holds true, it immediately follows that the radar received power is

$$P^{rx} = \frac{G_T^2 P_T G^2 {F^{tot}}^2 d_x^2 d_y^2 \eta_{RIS}^2 \lambda_0^2 \sigma}{r_1^4 r_2^4 (4\pi)^5}|\mathbf{1}_N^T\,\boldsymbol{\Sigma}\,\mathbf{1}_M|^4 \tag{6}$$

Leveraging (6), it is now possible to derive the SNR for a RIS-assisted sensing mode. To this end, let F_N be the noise figure of the radar receiver and B the radar bandwidth, then

$$\begin{aligned} \text{SNR} =& \frac{G_T^2 P_T G^2 {F^{tot}}^2 d_x^2 d_y^2 \eta_{RIS}^2 \lambda_0^2 \sigma}{r_1^4 r_2^4 (4\pi)^5 k T_0 B F_N}|\mathbf{1}_N^T\,\boldsymbol{\Sigma}\,\mathbf{1}_M|^4 = \\ & \frac{G_T^2 P_T G^2 {F^{tot}}^2 d_x^2 d_y^2 \eta_{RIS}^2 \lambda_0^2 \tau \sigma}{r_1^4 r_2^4 (4\pi)^5 k T_0 F_N}|\mathbf{1}_N^T\,\boldsymbol{\Sigma}\,\mathbf{1}_M|^4, \end{aligned} \tag{7}$$

where k is Boltzmann's constant, T_0 the standard temperature, i.e., 290 K, and τ the pulse length. Remarkably, the provided SNR expression in terms of the pulse length τ holds true for both unmodulated and modulated pulses.

Usually, a radar system transmits multiple pulses to probe the environment. Equation (7) can be used to determine the integrated SNR when a coherent burst of N_p pulses illuminates the target via a RIS. Specifically, if the RIS does not change its reflecting characteristics during the radar dwell-time, the RCS exhibits at most a burst-to-burst fluctuation, and the N_p echoes are combined through coherent integration processing, the resulting coherently integrated SNR is given by

$$\text{SNR}_c(N_p) = \text{SNR}N_p, \tag{8}$$

where N_p is the coherent integration gain.

Expression (8) represents an idealized form of the target SNR, because phenomena that reduce the received useful signal power, producing SNR loss, are neglected. Otherwise stated, a more realistic SNR expression is

$$\text{SNR}_c(N_p) = \frac{\text{SNR}N_p}{L_s}, \tag{9}$$

where L_s constitutes the total system loss [45]. This last term can be also recast as

$$L_s = L_t L_{atm} L_r L_{sp} L_{ris} \tag{10}$$

with

- L_t the transmit loss [45], [56]: it is related to the signal

attenuation due to transmitter devices and components, such as circulators and waveguides;
- $L_{atm} = L_{atm_1} L_{atm_2}$ the atmospheric loss [45], [56], [57]: it accounts for electromagnetic wave absorption due to fog, rain, snow, and water vapor to mention a few (L_{atm_i}, $i = 1, 2$, refers to the two-way propagation loss in sub-region i);
- L_r the receiver loss [45], [56]: it represents the receive-side counterpart to L_t;
- L_{sp} the signal processing loss [45]: it accounts for the coherent integration gain reduction due to range/Doppler straddle loss, and useful signal mismatches (e.g. from possible I/Q imbalance and oscillators phase noise); besides, it describes sub-optimal processing, e.g., CFAR detectors and range/Doppler tapering;
- L_{ris} the RIS loss [5]: it refers to RIS-patches power absorption as well as mismatches between nominal and actual reflecting coefficients, resulting from quantization errors.

Based on eqs. (7) and (9), it is immediate to obtain the average power form of the radar range equation for a RIS-assisted sensing mode. In this respect, note that

$$P_T = P_{avg} \frac{T}{\tau}, \tag{11}$$

where P_{avg} is the average transmit power. Hence, it follows that (9) can be cast as

$$\text{SNR}_c = \frac{G_T^2 G^2 {F^{tot}}^2 d_x^2 d_y^2 \eta_{RIS}^2 \lambda_0^2 \sigma P_{avg} T_d}{r_1^4 r_2^4 (4\pi)^5 k T_0 F_N L_s} |\mathbf{1}_N^T \, \boldsymbol{\Sigma} \, \mathbf{1}_M|^4, \tag{12}$$

which clearly highlights that the longer the dwell time the higher the SNR, as per a conventional radar system.

Before concluding this section, two interesting remarks are provided.

Remark 1. The SNR depends on $|\mathbf{1}_N^T \, \boldsymbol{\Sigma} \, \mathbf{1}_M|^4$, in the following referred to as RIS-induced pattern, which is a function of the RIS angular location w.r.t. the radar, i.e., $\left(\theta_{RIS}^R, \phi_{RIS}^R\right)$, the target angular location w.r.t. RIS, i.e., $\left(\theta_{RIS}^{T_a}, \phi_{RIS}^{T_a}\right)$, and the RIS programmable reflecting coefficients, i.e., $\boldsymbol{\Gamma}$. The RIS-induced pattern is upper bounded by $(NM)^4$ because the amplitude of each entry of $\boldsymbol{\Gamma}$ is assumed smaller than or equal to one (any RIS-patch is modeled as a passive component) and the entries of $\boldsymbol{S}_i$, for $i = 1, 2$, have a constant modulus. The mentioned bound is achieved when $\boldsymbol{\Gamma} = \boldsymbol{S}_1{}^* \odot \boldsymbol{S}_2{}^*$, which is tantamount to coherently aligning the phases of all the contributions reflected from the RIS, by compensating the phases terms of $\boldsymbol{S}_1 \odot \boldsymbol{S}_2$. However, while $\left(\theta_{RIS}^R, \phi_{RIS}^R\right)$ is fixed and known with a high accuracy, only a nominal value of $\left(\theta_{RIS}^{T_a}, \phi_{RIS}^{T_a}\right)$ is available, which coincides with the steering direction of the RIS beam in sub-region 2. This can determine a mismatch between the target actual angular position and the RIS steering direction which can lead to a SNR loss. To shed light on the effects of the mentioned mismatches and to provide as a by-product, guidelines for the definition of a sequential scanning protocol in sub-region 2 (in particular how to space the pointing directions), let us assume that $\boldsymbol{\Gamma} = \bar{\boldsymbol{S}}_1{}^* \odot \bar{\boldsymbol{S}}_2{}^*$ with $\bar{\boldsymbol{S}}_1 = \boldsymbol{p}_1(\theta_1, \phi_1)\boldsymbol{p}_2(\theta_1, \phi_1)^T$ and $\bar{\boldsymbol{S}}_2 = \boldsymbol{p}_1(\theta_2, \phi_2)\boldsymbol{p}_2(\theta_2, \phi_2)^T$. As shown in Appendix A, the RIS-induced pattern boils down to

$$|\mathbf{1}_N^T \, \boldsymbol{\Sigma} \, \mathbf{1}_M|^4 = \left|\frac{\sin(\Delta\kappa_u \pi N)}{\sin(\Delta\kappa_u \pi)}\right|^4 \left|\frac{\sin(\Delta\kappa_v \pi M)}{\sin(\Delta\kappa_v \pi)}\right|^4 \tag{13}$$

where

$$\Delta\kappa_u = \frac{d_x}{\lambda_0}\left[(u_{RIS}^{T_a} - u_2) + (u_{RIS}^R - u_1)\right], \tag{14a}$$

and

$$\Delta\kappa_v = \frac{d_y}{\lambda_0}\left[(v_{RIS}^{T_a} - v_2) + (v_{RIS}^R - v_1)\right], \tag{14b}$$

with

$$u_i = \sin(\theta_i)\cos(\phi_i), \; i = 1, 2, \tag{15a}$$

$$v_i = \sin(\theta_i)\sin(\phi_i), \; i = 1, 2, \tag{15b}$$

and, for $\beta \in \{R, T_a\}$,

$$u_{RIS}^\beta = \sin(\theta_{RIS}^\beta)\cos(\phi_{RIS}^\beta), \tag{16a}$$

$$v_{RIS}^\beta = \sin(\theta_{RIS}^\beta)\sin(\phi_{RIS}^\beta). \tag{16b}$$

Equation (13) suggests that the RIS-induced pattern exhibits a factorized form w.r.t. the variables $\Delta\kappa_u$ and $\Delta\kappa_v$, which depends on the offsets of the directional cosines. Specifically, $\Delta\kappa_u$ is the sum of the offsets in the u-direction $(u_{RIS}^R - u_2)$ and $(u_{RIS}^T - u_1)$, associated with the radar-RIS path and the RIS-target path, respectively, times $\frac{d_y}{\lambda_0}$. Analogously, $\Delta\kappa_v$ accounts for the offsets in the v-direction.

Each factor is the fourth power of a specific Dirichlet kernel. Precisely, the pattern in the $\Delta\kappa_u$ domain presents a maximum at $\Delta\kappa_u = 0$, with a $\frac{2}{N}$ null-to-null mainlobe width. Besides, in each unitary-period, it exhibits $N - 2$ sidelobes whose width is $\frac{1}{N}$. Similarly, in the $\Delta\kappa_v$ domain, the mainlobe is centered at $\Delta\kappa_v = 0$ with a $\frac{2}{M}$ width, and $M - 2$ sidelobes of width $\frac{1}{M}$ appear in each unitary-period.

Based on the above considerations, it follows that the maximum value of the RIS-induced pattern is appearing in $\theta_{RIS}^R = \theta_1$, $\phi_{RIS}^R = \phi_1$, $\theta_{RIS}^{T_a} = \theta_2$, and $\phi_{RIS}^{T_a} = \phi_2$. Let us now suppose that the phase-matching condition holds true only in sub-region 1. Then, (13) implies that the RIS-induced pattern, in sub-region 2, is the same as for a uniform rectangular disposed in the RIS plane (with N and M antennas along the x-axis and y-axis in CRS_2, respectively) which is electronically steered in the direction θ_2 and ϕ_2. As a consequence, the azimuth and elevation single-side beamwidths $\bar{\phi}_{RIS}$ and $\bar{\theta}_{RIS}$ can be obtained as in [58]; for instance, if $d_x = d_y = \frac{\lambda_0}{2}$ and $\theta_2 = 0$, i.e., the RIS-patches are steered in the broadside direction, with $\bar{\phi}_{RIS} = 0.891/N$ and $\bar{\theta}_{RIS} = 0.891/M$ the 12 dB beamwidths of the RIS.

Finally, it is worth pointing out that eq. (13) provides a guideline to tile the coverage area in sub-region 2 with RIS beams (i.e., appropriate selections of θ_2 and ϕ_2), also accounting for the maximum acceptable SNR angular loss and the dwell time, see (12).

Remark 2. An interesting interpretation of eqs. (7) and (9) is now provided in terms of an *equivalent* monostatic radar

configuration. Specifically, eq. (9) can be cast as [45]

$$\text{SNR}_c(N_p) = \frac{G_T^{eq\,2} P_T \lambda_0^2 \sigma^{eq} N_p \tau}{r_{eq}^4 (4\pi)^3 k T_0 F_N L_s^{eq}}, \tag{17}$$

where

$$\sigma^{eq} = \sigma, \tag{18}$$

$$G_T^{eq} = G_T G\, \eta_{RIS}\, N^2 M^2, \tag{19}$$

$$r_{eq} = r_1 + r_2 \tag{20}$$

is the equivalent radar-target distance, and

$$L_s^{eq} = L_t L_{atm} L_r L_{sp}^{eq} L_{ris}^{eq} L_{geom}, \tag{21}$$

with

$$L_{sp}^{eq} = L_{sp} \frac{(NM)^4}{F^{tot\,2} |\mathbf{1}_N^T \boldsymbol{\Sigma}\, \mathbf{1}_M|^4}, \tag{22a}$$

$$L_{ris}^{eq} = L_{ris} \pi^2, \tag{22b}$$

$$L_{geom} = \left(\frac{2}{\frac{\sqrt{d_x d_y}}{r_1} + \frac{\sqrt{d_x d_y}}{r_2}} \right)^4. \tag{22c}$$

Interestingly, L_{geom} can be also expressed as

$$L_{geom} = \left(\frac{\left(\frac{r_1^{-1} + r_2^{-1}}{2} \right)^{-1}}{\sqrt{d_x d_y}} \right)^4, \tag{22d}$$

which coincides with the fourth power of the harmonic mean between the path lengths in the two sub-regions, i.e., $(1/2\ (1/r1 + 1/r2))^{-1}$, normalized to the geometric mean between d_x and d_y, i.e., $\sqrt{d_x d_y}$, which represents the characteristic size of each RIS-patch. As consequence, L_{geom} accounts for the loss induced by a different propagation mechanism that relies on the reflection of the waves from RIS-patches, each with area $d_x d_y$.

A pictorial representation of the *equivalent* monostatic configuration associated with the RIS-assisted sensing system is depicted in Fig. 5. Therein, a 2D situation is reported and the azimuth beamwidth of the equivalent monostatic system, i.e. $\bar{\phi}_{eq}$, is set so that the cross-range resolution at the equivalent point of interest, i.e., $\bar{\phi}_{eq}(r_1 + r_2)$, is the same as that of the RIS-assisted system at the point $\boldsymbol{s}_T$, i.e., $\bar{\phi}_{RIS}\, r_2$.

IV. Radar Equation for Clutter Interference

This section is devoted to the computation of the SCR for the operative mode in sub-region 2. Surface clutter and volume clutter are considered. In the first case, the SCR is evaluated for pulse length-limited and beamwidth-limited geometry.

A. Surface clutter: pulse length-limited

The illuminated area A_c depends on the RIS azimuth beamwidth $\bar{\phi}_{RIS}$ and the length of the pulse τ measured along the surface; specifically, [59]

$$\begin{aligned} A_c &= 2\, r_2 \left(\frac{c\tau}{2} \right) \tan\left(\frac{\bar{\phi}_{RIS}}{2} \right) \sec\psi \\ &\simeq r_2 \left(\frac{c\tau}{2} \right) \bar{\phi}_{RIS} \sec\psi, \end{aligned} \tag{23}$$

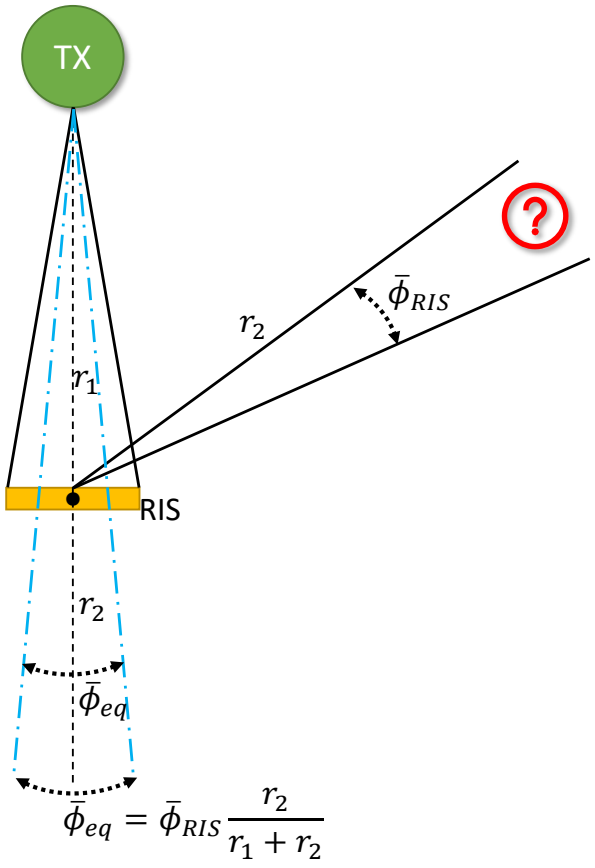

Fig. 5. A representation of the *equivalent* monostatic configuration associated with the RIS-assisted surveillance system.

where ψ is the grazing angle and the tangent approximation relies on the small angle assumption for $\bar{\phi}_{RIS}$. Besides, in the case of a modulated pulse, in place of $\frac{c\tau}{2}$, the actual range resolution δ_r must be employed.

Letting σ_0 the surface reflectivity, the clutter power at the radar is thus given by

$$\begin{aligned} C &= \frac{G_T^2 P_T G^2 F^{tot\,2} d_x^2 d_y^2 \eta_{RIS}^2 \lambda_0^2 A_c \sigma_0}{r_1^4 r_2^4 (4\pi)^5} |\mathbf{1}_N^T \boldsymbol{\Sigma}\, \mathbf{1}_M|^4 = \\ &\frac{G_T^2 P_T G^2 F^{tot\,2} d_x^2 d_y^2 \eta_{RIS}^2 \lambda_0^2 c\tau \bar{\phi}_{RIS}\, \sigma_0\, \sec\psi}{r_1^4 r_2^3 2^{11} \pi^5} |\mathbf{1}_N^T \boldsymbol{\Sigma}\, \mathbf{1}_M|^4. \end{aligned} \tag{24}$$

It follows that the SCR is given by

$$\text{SCR}_{pll} = \frac{2\, \cos\psi}{r_2\, c\, \tau\, \bar{\phi}_{RIS}} \frac{\sigma}{\sigma_0}, \tag{25}$$

which highlights that the SCR decreases according to an inverse linear law with the r_2 distance between the RIS and the target. Besides, the SCR does not depend on the r_1 distance between the radar and the RIS, nor on the radar transmit/receive beamwidths. Moreover, the SCR is inversely proportional to RIS azimuth beamwidth $\bar{\phi}_{RIS}$, which frames the size of the radar cell in sub-region 2.

B. Surface clutter: beamwidth-limited

Assuming a circular beam, the illuminated area is [59]

$$A = \pi\, r_2^2\, \tan^2\left(\frac{\bar{\phi}_{RIS}}{2}\right) \simeq \frac{\pi\, r_2^2\, \bar{\phi}_{RIS}^2}{4}, \tag{26}$$

where again the small angle approximation for $\bar{\phi}_{RIS}$ has been invoked. As a consequence, the clutter power at the radar is

$$C = \frac{G_T^2 P_T G^2 {F^{tot}}^2 d_x^2 d_y^2 \eta_{RIS}^2 \lambda_0^2\, \bar{\phi}_{RIS}^2 \sigma_0}{r_1^4 r_2^2\, 2^{12}\, \pi^4} |\mathbf{1}_N^T\, \mathbf{\Sigma}\, \mathbf{1}_M|^4 \tag{27}$$

and the resulting SCR can be cast as

$$\text{SCR}_{bwl} = \frac{4}{\pi\, r_2^2 \bar{\phi}_{RIS}^2} \frac{\sigma}{\sigma_0}. \tag{28}$$

The same considerations in the pulse length case apply except the dependence over r_2 and ϕ_{RIS} which follow now a $1/r_2^2$ and $1/\phi_{RIS}^2$ law, respectively.

C. Volume clutter

In this sub-section, the SCR expression for volume clutter is obtained. Specifically, the scatterers are assumed uniformly distributed across the illuminated volume [45]

$$\begin{aligned} V_c &= \pi\, r_2^2 \left(\frac{c\tau}{2}\right) \tan\left(\frac{\bar{\phi}_{RIS}}{2}\right) \tan\left(\frac{\bar{\theta}_{RIS}}{2}\right) \\ &\simeq \frac{\pi}{4}\left(\frac{c\tau}{2}\right) r_2^2 \bar{\phi}_{RIS} \bar{\theta}_{RIS}, \end{aligned} \tag{29}$$

where $\bar{\theta}_{RIS}$ denotes the elevation beamwidth of the RIS while the last approximation relies on the small angle assumption for $\bar{\phi}_{RIS}$ and $\bar{\theta}_{RIS}$. Again, for a modulated pulse, the range resolution δ_r must be used in lieu of $\frac{c\tau}{2}$. Therefore, the clutter power return is given by

$$\begin{aligned} C \;=\; & \frac{G_T^2 P_T G^2 {F^{tot}}^2 d_x^2 d_y^2 \eta_{RIS}^2 \lambda_0^2 V_c \gamma_0}{r_1^4 r_2^4 (4\pi)^5} |\mathbf{1}_N^T\, \mathbf{\Sigma}\, \mathbf{1}_M|^4 = \\ & \frac{G_T^2 P_T G^2 {F^{tot}}^2 d_x^2 d_y^2 \eta_{RIS}^2 \lambda_0^2\, c\tau\, \bar{\phi}_{RIS} \bar{\theta}_{RIS}\, \gamma_0}{r_1^4 r_2^2 2^{13} \pi^4} |\mathbf{1}_N^T\, \mathbf{\Sigma}\, \mathbf{1}_M|^4, \end{aligned} \tag{30}$$

where γ_0 is the volume reflectivity. As a consequence, the SCR for volume clutter is given by

$$\text{SCR}_v = \frac{8}{\pi\, c\, \tau\, r_2^2\, \bar{\phi}_{RIS} \bar{\theta}_{RIS}} \frac{\sigma}{\gamma_0}, \tag{31}$$

resulting in an inverse square law dependence on the r_2 distance between the RIS and the target. Similar to the surface clutter case, the distance between the radar and the RIS as well as the radar transmit/receive beamwidths do not affect the SCR. Finally, an inverse linear dependence with respect to both $\bar{\phi}_{RIS}$ and $\bar{\theta}_{RIS}$ is present, since the aforementioned parameters determine the size of the volume clutter cell.

V. Operation in Sub-Region 2 and Radar Echo Model

An example of a radar burst transmission for the operative mode in sub-region 2 is provided in Fig. 6. The first pulse (whose duration, as already said, is denoted by τ) is transmitted by the radar and reaches the RIS after a time lapse r_1/c. The interval $[\tau, 2r_1/c]$ represents an "idle" interval where radar transmission and reception from sub-region 2 is inhibited. The programmed surface re-directs the pulse to cover with a specific beam the desired portion of sub-region 2, via an appropriate phase steering. Then, a listening time starts where return signals are forwarded by the RIS toward the radar which performs data acquisition to form the fast-time slow-time matrix. The length of the listening time is $2R_{ua}/c$ with R_{ua} the maximum unambiguous range with respect to the RIS. Then after $2R_{ua}/c + 2r_1/c$ the second pulse is transmitted by the radar and the cycle continues until the end of the dwell. As discussed in **Remark 1** of Section III, the azimuth resolution is determined by the size and geometrical/physical properties of the RIS as well as by the radar wavelength.

To gather insights on the range and Doppler resolutions, the signal model for the echo induced by a target is now developed. To this end, let us denote by $s(t)$ the complex envelope of the narrow-band radar transmit signal, i.e.,

$$s(t) = \sum_{i=1}^{N_p} \sqrt{P_T}\, p(t - (i-1)T) e^{j2\pi f_0 t} \tag{32}$$

where $p(t)$ is a unit-energy baseband pulse of duration τ and bandwidth B, and $f_0 = \frac{c}{\lambda_0}$ is the carrier frequency (with c the speed of light).

A prospective target at location $\boldsymbol{s}_T$ (in sub-region 2) and velocity $\boldsymbol{v}_T$ produces a backscattered electric field toward the RIS, given by

$$\boldsymbol{E}_T^{RIS}(t) = \sum_{i=1}^{N_p} \alpha_1 p(t - \tau_1 - (i-1)T) e^{j2\pi(f_0 + f_{d_T})t} \boldsymbol{S}_2 \tag{33}$$

where $\tau_1 = \frac{r_1 + 2r_2}{c}$, $f_{dT} = 2\frac{v_{r,RIS}}{\lambda_0}$, with $v_{r,RIS} = \frac{(\boldsymbol{s}_{RIS} - \boldsymbol{s}_T)^T}{\|\boldsymbol{s}_{RIS} - \boldsymbol{s}_T\|} \boldsymbol{v}_T$ the component of the target velocity along the radial line from the RIS to the target; furthermore, $\alpha_1 = \sqrt{\frac{2Z_0 \mathcal{P}\sigma}{(4\pi L_1)}} e^{j\varphi_1}$, with L_1 the loss factor involved in the considered partial propagation path and φ_1 related to the phase responses of the radar transmit antenna, the RIS-patches, the target as well as the propagation path delays. Otherwise stated, $\boldsymbol{E}_T^{RIS}(t)$ is proportional to a delayed and frequency shifted version of the radar transmitted burst. The electric field in eq. (33) is thus focused toward the radar via the programmable reflecting coefficients $\mathbf{\Gamma}$, resulting, under the "stop-and-hop" assumption, into the target-induced radar received signal

$$s_R(t) = \sum_{i=1}^{N_p} \alpha p(t - \tau_0 - (i-1)T) e^{j2\pi(f_0 + f_{d_T})t} \tag{34}$$

where $\tau_0 = 2\frac{r_1 + r_2}{c}$ and $\alpha = Ae^{j\varphi}$ is a complex value with $A = \sqrt{P^{rx}}/\sqrt{L_t L_{atm} L_r L_{ris}}$ and φ encompassing all the phase terms.

According to the conventional and consolidated radar signal processing, the signal in eq. (34) is down converted to baseband and undergoes a matched filtering process w.r.t. the pulse $p(t)$, i.e., pulse compression. The pulse-compressed output-

This article has been accepted for publication in IEEE Transactions on Vehicular Technology. This is the author's version which has not been fully edited and content may change prior to final publication. Citation information: DOI 10.1109/TVT.2021.3102315

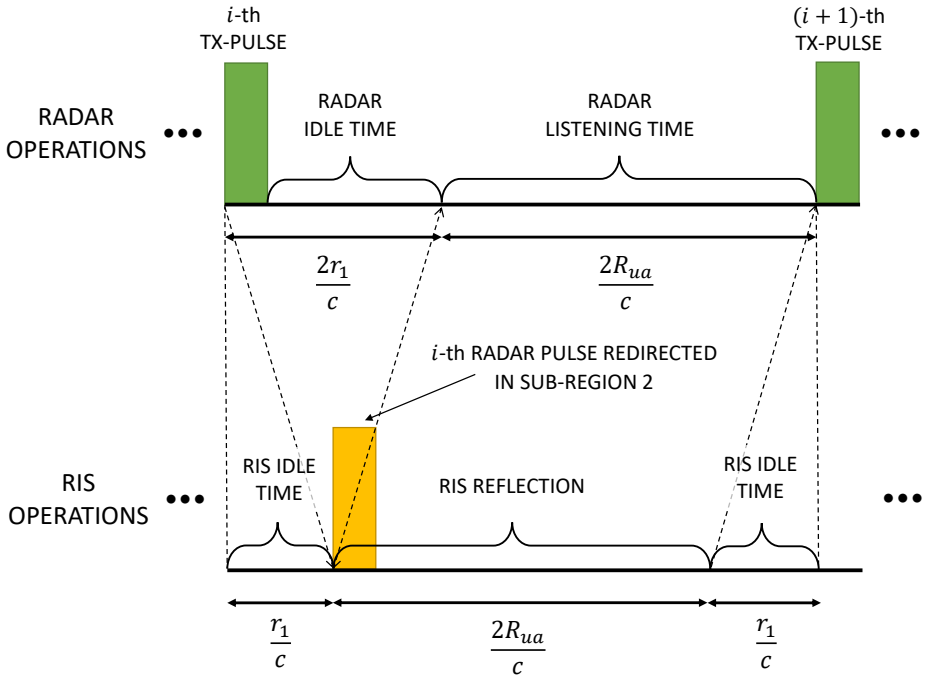

Fig. 6. An illustrative example of the radar burst transmission for the operative mode in sub-region 2.

signal is thus given by

$$z_R(t) = \sum_{i=1}^{N_p} \alpha \chi_p(t - \tau_0 - (i-1)T, f_{dT}) e^{j2\pi\nu_{dT}(i-1)} \quad (35)$$

where

- $\chi_p(t_1, f_d) = \int_{-\infty}^{\infty} p(t)p^*(t-t_1)e^{j2\pi f_d t}dt$ is the (complex) ambiguity function of the pulse waveform $p(t)$,
- $\nu_{dT} = f_{dT}T$ is the normalized target Doppler frequency.

Expression (35) can be further manipulated if $p(t)$ is Doppler tolerant, i.e., $\chi_p(t_1, f_{dT}) \simeq \chi_p(t_1, 0)$, at the Doppler frequencies of interest. In this case

$$z_R(t) \simeq \sum_{i=1}^{N_p} \alpha r_p(t - \tau_0 - (i-1)T) e^{j2\pi\nu_{dT}(i-1)} \quad (36)$$

where $r_p(t_1) = \chi_p(t_1, 0)$ is the autocorrelation function of $p(t)$. Now, observing that the functional forms of (35) and (36) are the same as those for a standard monostatic radar [60], it follows that two targets in region 2, located at $\boldsymbol{s}_{T1}$ and $\boldsymbol{s}_{T2}$ with Doppler frequencies f_{dT1} and f_{dT2}, respectively, can be distinguished in range if

$$\begin{aligned} &\left|(\|\boldsymbol{s}_{T1} - \boldsymbol{s}_{ris}\| + r_1) - (\|\boldsymbol{s}_{T2} - \boldsymbol{s}_{ris}\| + r_1)\right| \\ &= |r_2^1 - r_2^2| \geq \frac{c}{2B}, \end{aligned} \quad (37)$$

and in Doppler if

$$|f_{dT,1} - f_{dT,2}| \geq \frac{1}{N_p T}, \quad (38)$$

with r_2^k the distance between the RIS and the k-th target, $k = 1, 2$ Otherwise stated, the range and Doppler resolutions of the RIS-assisted radar are $\Delta R_{ris} = \frac{c}{2B}$ and $\Delta f_{d_{ris}} = \frac{1}{N_p T}$, respectively, where the target range $r_1 + r_2$ is composed by the fixed and known bias term r_1 plus the range $r_2 = \|\boldsymbol{s}_T - \boldsymbol{s}_{ris}\|$ computed w.r.t. CRS_2, and Doppler frequency refers to the target radial velocity w.r.t. CRS_2. As a consequence, as in sub-region 1, the range resolution in sub-region 2 is ruled by the bandwidth B of the radar waveform. Moreover, the Doppler resolution is inversely proportional to the dwell time $N_p T$.

Before concluding this section, let us observe that eq. (36), together with the derived range resolution, allow for the construction of the fast-time slow-time data matrix $\boldsymbol{D}$ corresponding to sub-region 2. Specifically, let $\bar{z}_R(t)$ be the radar received signal after down-conversion and pulse compression. Then the (h, l)-th entry of $\boldsymbol{D}$, $h = 1, \ldots, h_{max} + 1$, $l = 1, \ldots N_p$, is given by

$$\boldsymbol{D}(h, l) = \bar{z}_R \left(2\frac{r_1 + r_2^b}{c} + \frac{(h-1)}{B} + (l-1)T \right), \quad (39)$$

where r_2^b is the minimum operative range in sub-region 2 and h_{max} such that $r_1 + r_2^b + h_{max}\Delta R_{ris} = R_{ua}$.

This represents the data block used by the radar to perform any successive signal processing such as MTI, pulse Doppler, CFAR, etc.

VI. Numerical Results

In this section, numerical examples are provided to assess the performance of the proposed N-LOS modality in terms of SNR and P_d. All the simulations have been performed via MATLAB 2020a running on a desktop PC with an Intel Core i5 processor and 16 GB of RAM. Besides, an analysis on the SNR loss w.r.t. a clairvoyant monostatic configuration is provided too. To this end, three different RISs (each comprising $N \times M$ elements) with $N = M \in \{101, 133, 201\}$,

are considered. Therefore, assuming an inter-element space of $\lambda_0/2 = 0.015$ m, the area occupied by each of the considered RISs is approximately equal to 1.5 m $\times$ 1.5 m, $2.0\text{m}\times2.0\text{m}$, and $3.0\text{m}\times3.0\text{m}$, respectively. As a consequence, the corresponding far field distance (FFD) is 152.91 m, 265.15 m, and 605.60 m, respectively, where FFD is computed as $r_{FFD} = 2(\max(d_x N,\ d_y M))^2/\lambda_0$. The normalized RIS-patch power radiation pattern is modeled as

$$F(\theta_R) = \begin{cases} \cos^{1.5}(\theta_R) & \text{if } \theta_R \in [0, \pi/2] \\ 0 & \text{otherwise} \end{cases}, \qquad (40)$$

which is suitable for an antenna isotropic in azimuth, operating in an elevation range (w.r.t. the RIS) of $[0, \pi/3]$ [45]. As to the target, a typical micro UAV, characterized by a RCS of 0.02 m^2, is considered. The values of the system parameters involved in the analyzed case studies are summarized in Table I. Moreover, Table II reports the dwell times (assuming a maximum unambiguous range of 10 Km, i.e., a Pulse Repetition Time (PRT) of 66.71 μs) corresponding to the different number of pulses used to evaluate the SNR and P_d. All of them are compatible with a range resolution of 15 m which can be obtained with a modulated pulse whose bandwidth B is 10 MHz. It is also important to remark that B poses a constraint to the size of the RIS because of the narrowband assumption which can be no longer met when $\max(d_x N, d_y M) > 3.0$ m.

TABLE I
SIMULATION PARAMETERS

Parameter	Value
N, M	$\{101, 133, 201\}$
d_x, d_y	$\lambda_0/2$
η_{RIS}	0.8
σ	0.02 m^2
r_1	1000 m
f	10 GHz
N_p	$\{8, 16, 32, 64, 128\}$
τ	1.5×10^{-6} s
P_t	26 dBW
G_t	38 dB
G	4 dB
L_{tot}	6 dB
F_N	2.5 dB
$F^R(\theta_R, \phi_R)$	0 dB

TABLE II
NUMBER OF PULSES AND DWELL TIME ASSUMING AN UNAMBIGUOUS RANGE OF 10KM

Number of Pulses	Dwell Time
8	0.53 ms
16	1.07 ms
32	2.13 ms
64	4.27 ms
128	8.54 ms

Fig. 7 reports the RIS induced pattern pertaining to (13) (normalized to the peak value $(NM)^4$) versus $\theta_{RIS}^{T_a}$ and $\phi_{RIS}^{T_a}$, for three different RIS sizes (see Table I) and two diverse pointing directions in sub-region 2. Specifically, in all the plots the phase-matching condition holds true in sub-region 1, i.e., $\theta_1 = \theta_{RIS}^R$ and $\phi_1 = \phi_{RIS}^R$, and Figs. 7(a), 7(b), and 7(c) refer to $\theta_2 = \phi_2 = 0$, whereas Figs. 7(d), 7(e), and 7(f) correspond to $\theta_2 = 10^\circ$, $\phi_2 = 20^\circ$. Furthermore, Figs. 7(a), 7(d) consider $N = M = 201$, while $N = M = 133$ and $N = M = 101$ are exploited in Figs. 7(b), 7(e) and Figs. 7(c), 7(f), respectively.

Inspection of the figures unveils that the maximum pattern value is achieved when the target is located along the RIS pointing direction, in accordance with the theoretical achievements of Section III. It can also be observed that, regardless of the RIS size, the beamwidths widen as the RIS is steered toward a direction far from the boresight, a well-known phenomenon in Active Electronically Scanned Arrays (AESAs) [58], [61]. Lastly, the larger the RIS size the narrower the beam in sub-region 2, being the reflected energy focused better and better in the desired looking direction.

Fig. 8 displays the $\text{SNR}_c(N_p)$ (defined in (9)) versus r_2 assuming the three different RIS configurations of Table I and different choices for the number of pulses. The corresponding FFD ranges are also superimposed to the figure. Not surprisingly, the SNR decreases as the distance between the target and the RIS increases, whereas an improvement is connected with a larger number of RIS elements as well as to an increased number of coherently integrated pulses. Nevertheless, a large RIS area corresponds to an increased FFD as well as to a more complex RIS control. On one hand this underpins a trade-off between the SNR level and the complexity of the scenario while on the other it suggests the development of new radar processing strategies for near-field operation if large RIS dimensions are required. Furthermore, a crucial role in the SNR budget is played by the number of pulses (and hence by the dwell time on the target) with SNR improvement up to 12 dB when $N_p = 128$ w.r.t. the $N_p = 8$ case. Finally, if a mini UAV ($\sigma = 0.2$ m^2) is considered as prospective target in place of the micro UAV, an improvement of 10 dB in the resulting SNR occurs.

Fig. 9 displays SCR and SNR using a modulated pulse with a bandwidth $B = 10$ MHz (which corresponds to $\delta_r = 15$ m) versus r_2 assuming the three different RIS configurations of Table I (the corresponding FFD ranges are superimposed to the figure). Fig. 9 (a) reports the case of surface clutter in urban terrains environment, i.e., $\sigma_0 = -18$ dB [45]. The range transitions between bandwidth-limited and pulse-length limited clutter model, i.e., $r_2\ \bar{\phi}_{RIS} \geq \frac{4\delta_r}{\pi\sqrt{1-H_{RIS}^2/r_2^2}}$ are marked with filled circles, assuming a RIS height, w.r.t. the target, of $H_{RIS} = 25$ m. The volume clutter case is analyzed in Fig. 9 (b), with SCR_v computed assuming heavy rain clutter, i.e., $\gamma_0 = -53$ dB/m [45].

As expected, the farther the target, the lower the SCR in all the considered cases, with performance gains resulting from a larger number of RIS elements. Indeed, the larger the number of RIS elements, the narrower the elevation and azimuth beamwidths, and thus the lower the clutter power. The results

This article has been accepted for publication in IEEE Transactions on Vehicular Technology. This is the author's version which has not been fully edited and content may change prior to final publication. Citation information: DOI 10.1109/TVT.2021.3102315

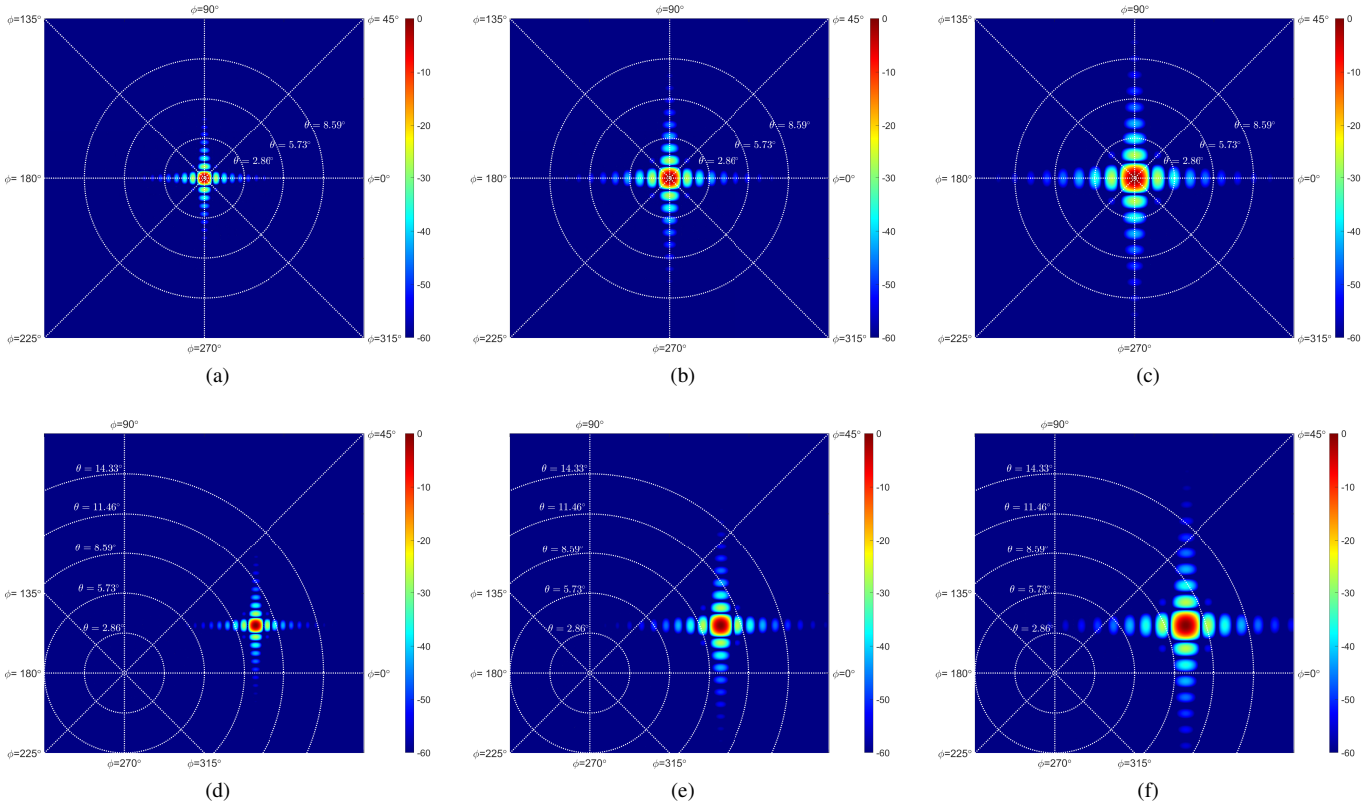

Fig. 7. Normalized RIS induced pattern versus $\theta^{T_a}_{RIS}$ and $\phi^{T_a}_{RIS}$ assuming $r_1 = 1000$ m and $r_2 = 1500$ m. Figs. (a) and (d) refer to $N = M = 201$, Figs. (b) and (e) $N = M = 133$, whereas Figs. (c) and (f) $N = M = 101$. Besides, $\theta_2 = \phi_2 = 0°$ is considered in Figs. (a), (b) and (c), whereas $\theta_2 = 10°$, $\phi_2 = 20°$ is assumed in Figs. (d), (e) and (f).

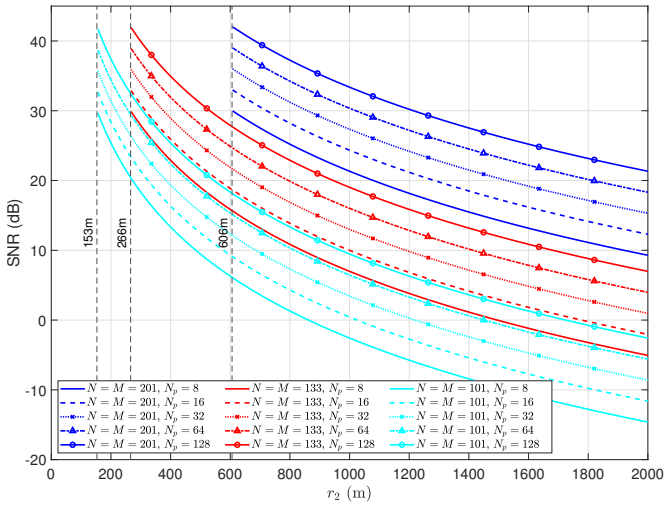

Fig. 8. SNR versus r_2 for different RIS sizes, number of pulses, and the parameters of Table I. Moreover, $\theta_1 = \theta^R_{RIS} = 30°$, $\phi_1 = \phi^R_{RIS} = 20°$, $\theta_2 = \theta^{T_a}_{RIS} = 0°$, and $\phi_2 = \phi^{T_a}_{RIS} = 0°$.

show that for the analyzed RIS-target distances, the SCR computed assuming surface clutter is significantly lower than the SNR. Besides, inspection of the curves assuming volume rain clutter, see Fig. 9 (b), highlight the $1/r_2^4$ dependency law of the SNR w.r.t. the RIS-target distance as compared with the inverse square law dependency of SCR_v on r_2.

Figs. 10 reports the P_d versus r_2 for a non fluctuating target, i.e., the target RCS is a deterministic parameter (also called a Swerling 0 (SW0) model), whereas Fig. 11 refers to a SW1 target, i.e., the RCS is drawn from an exponential distribution with a scan-to-scan decorellation. Figs. 10(a) and 11(a) refer to $\text{P}_{FA} = 10^{-4}$, whereas Figs. 10(b) and 11(b) consider $\text{P}_{FA} = 10^{-6}$. Specifically, denoting by Q_M the Generalized Marcum Q function, the P_d for the two analyzed cases is given by [45], [62]

$$\text{P}_{\text{d},SW0} = Q_M\left(\sqrt{2\ \text{SNR}_c}, \sqrt{-2\ \ln(\text{P}_{FA})}\right) \tag{41}$$

and

$$\text{P}_{\text{d},SW1} = \text{P}_{FA}{}^{(1/(1+\text{SNR}_c))}, \tag{42}$$

respectively.

As expected, the plots highlight that the higher r_2, the lower the P_d being SNR_c worse and worse. Moreover, the detectability of a SW1 target is more challenging than for a SW0 target. For instance, assuming $\text{P}_{FA} = 10^{-4}$, $N = M = 133$, and $N_p = 64$, P_d levels greater than 0.9 are achievable up to 1250 m, whereas a maximum range reduction close to 500 m is experienced for a SW1 counterpart. Besides, as P_d decreases, the performance gap between the SW0 and SW1 cases reduces and (as already well known) for low detection rates the fluctuation is beneficial. Finally, assuming $\text{P}_{FA} = 10^{-6}$ determines a further performance degradation of about 100 m at $\text{P}_\text{d} = 0.9$ w.r.t. the $\text{P}_{FA} = 10^{-4}$ case.

Fig. 12 displays the SNR Loss (L_{SNR}) w.r.t. a clairvoyant monostatic configuration, that assumes the absence of the

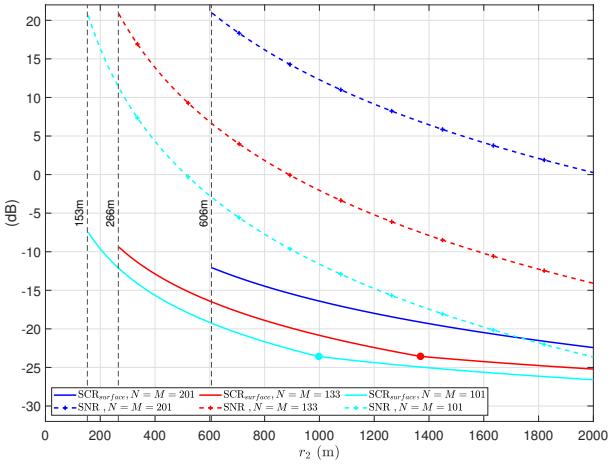

(a)

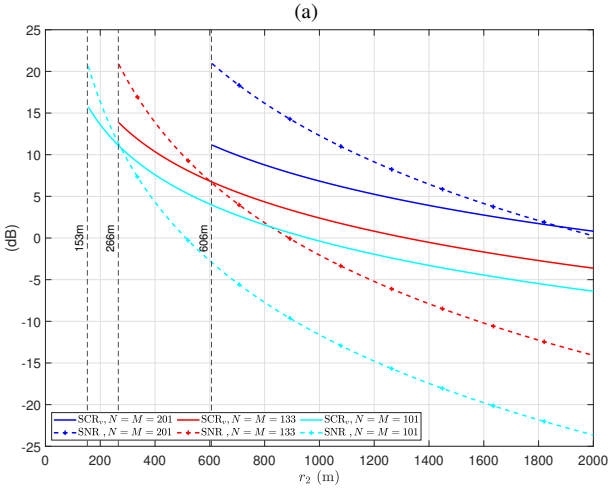

(b)

Fig. 9. Comparison between SCR and SNR versus r_2 for different RIS sizes and the parameters of Table I. Specifically, (a) considers surface clutter assuming $\sigma_0 = -18$ dB, whereas in (b) the volume clutter case is analyzed assuming $\gamma_0 = -53$ dB/m. The filled circles in (a) denote the transition between beamwidth-limited and pulse length-limited clutter condition.

blockage (i.e, the presence of the LOS path). Specifically, $\mathrm{L}_{SNR} = \mathrm{SNR}^m/\mathrm{SNR}$, with SNR^m pertaining to the clairvoyant system, is computed considering two different range scenarios. The former entails a target located at a range r_1+r_2 and the corresponding SNR^m is denoted by SNR_1^m. The latter considers a target positioned at $\sqrt{r_1^2+r_2^2}$ and the related SNR^m is indicated as SNR_2^m.

Also, Fig. 12(a), 12(b), and 12(c) refer to $r_1 = 500, 750, 1000$ m, respectively. As expected, the farther the target, the larger the L_{SNR} in all the analyzed cases. Clearly, regardless of the distance between the radar and the RIS, a somewhat significant loss is experienced w.r.t. the clairvoyant monostatic system. This is an important point and is a consequence of the two-way double-hop link established via the RIS link and surface parameters. Consequently, this could pose a limit to the maximum achievable radar detection range and relegates the new operational mode to quite short-range applications, especially for small size RISs. On the other hand, inspection of the figure corroborates that the use of a large RIS reduces the L_{SNR} with the drawback of an increased FFD distance and a higher RIS-controller complexity.

The last analysis in Fig. 13 evaluates the Scanning Loss $1/F^2(\theta_R)$. The curve highlights the capability of the RIS to scan elevation angles up to 45° with a loss smaller than 5 dB. Specifically, for $\theta_R \leq 20^\circ$ the loss is quite negligible, otherwise a proper compensation via an increased dwell time (dwell-time diversity) has to be granted to guarantee the desired performance level.

VII. Conclusion

In this paper the use of RIS technology is proposed to address radar surveillance in N-LOS conditions. A new sensing mode is developed via the formation of an artificial and favorable propagation environment established via the modulation of RIS parameters. For this operational regime the radar equation is laid down accounting for the artificially induced two-way and double-hop channel as well as the effects of the reflecting surface. Expressions for SNR and SCR (both for surface and volume clutter) are determined. Besides, the data acquisition procedure for N-LOS operation is discussed together with the resolution issues in the range, angle, and Doppler domains. A numerical analysis is carried on in terms of SNR, detection performance, and SNR loss with respect to a LOS monostatic geometry. The impact of the RIS size and system parameters is assessed corroborating the theoretical capability of the new framework to handle N-LOS short-range scenarios.

Nevertheless, it is worth observing that, albeit the potentialities, it is still necessary a complete understanding of the drawbacks connected with the employment of RIS which is a technology still in a maturing stage. Needless to say, even if plenty of research has been developed especially within the communication community, further efforts are required to ponder the pros and cons. Undoubtedly, it should be reckoned that from a theoretical point of view the use of RIS can represent a fertile research field giving new degrees of freedom for system optimization. As a consequence, the RIS topic is expected (in the authors' opinion) to flourish also in the radar context. In this respect, there are diverse radar applications which could benefit from this paradigm. Among them it is of interest to consider the joint use of natural multipath and the artificial (ad-hoc) multipath determined by the RIS to boost the performance of the "around the corner radar" [40]. Besides, RIS can also represent key elements for the cognitive radar architecture [63], i.e. another level of flexibility which can be adapted based on the perception-action cycle. In other words, by leveraging perception outputs, the radar can change the RIS parameters establishing a favorable propagation/sensing scenario via specific target-clutter illuminations both in terms of beam steering (size and direction) and polarization of the electromagnetic wave. Finally, the definition of RIS reflection coefficients selection strategies endowing robustness to the RIS-assisted radar with respect to unavoidable surface imperfections is, without doubt, a future research avenue worth of investigation.

This article has been accepted for publication in IEEE Transactions on Vehicular Technology. This is the author's version which has not been fully edited and content may change prior to final publication. Citation information: DOI 10.1109/TVT.2021.3102315

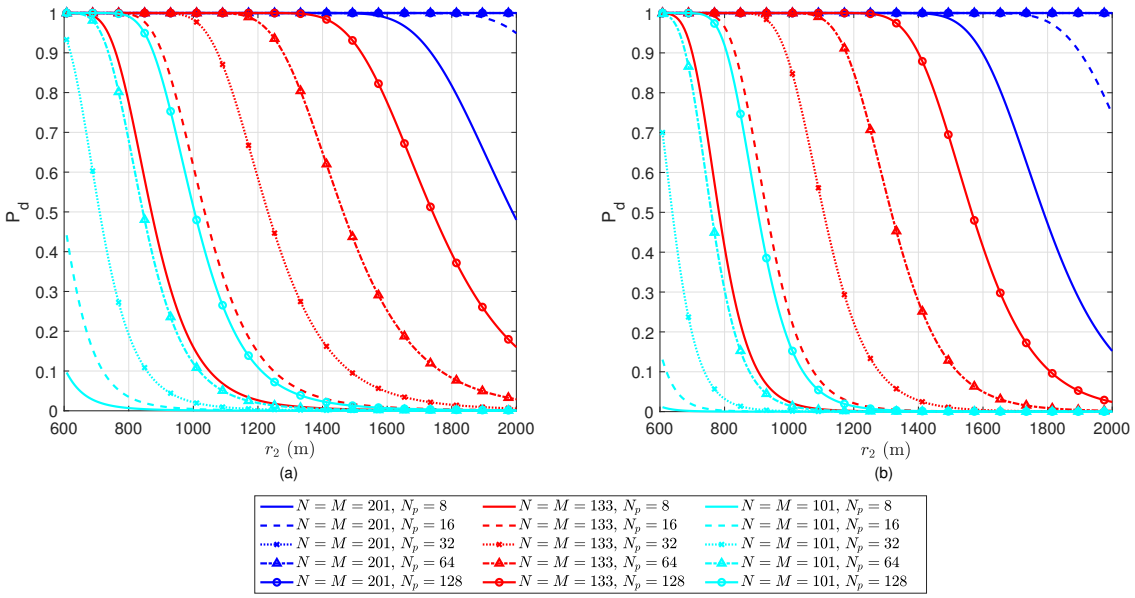

Fig. 10. $\mathrm{P_d}$ versus r_2 for a SW0 target case and different RIS sizes as well as number of pulses (see Table I). Therein, $\theta_1 = \theta_{RIS}^{R} = 30°$, $\phi_1 = \phi_{RIS}^{R} = 20°$, $\theta_2 = \theta_{RIS}^{T_a} = 0°$, $\phi_2 = \phi_{RIS}^{T_a} = 0°$, and in (a) $\mathrm{P}_{FA} = 10^{-4}$ while in (b) $\mathrm{P}_{FA} = 10^{-6}$.

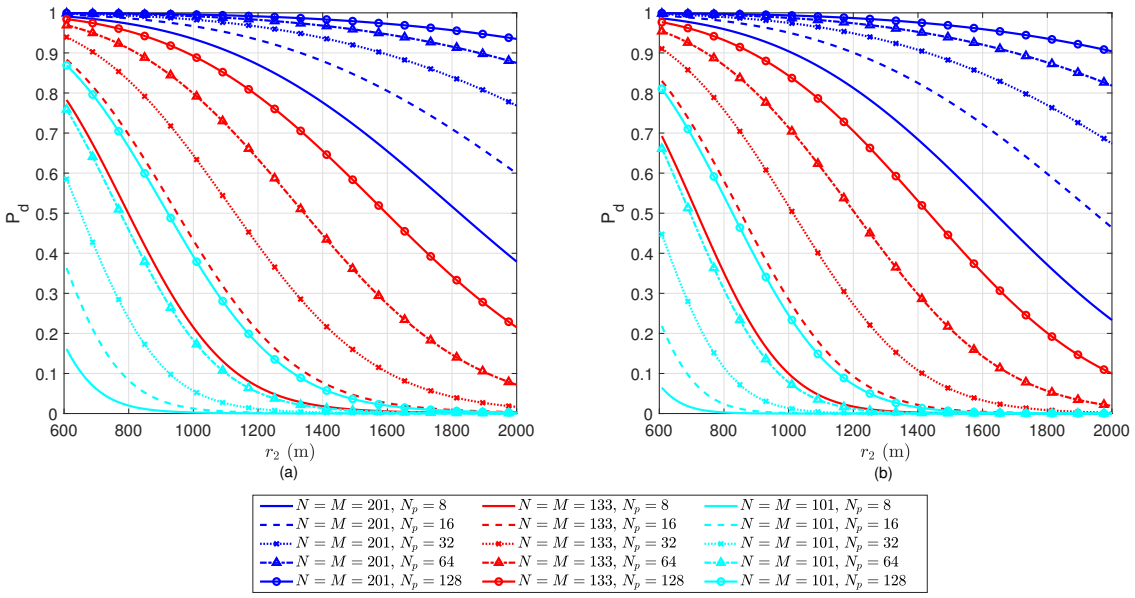

Fig. 11. $\mathrm{P_d}$ versus r_2 for a SW1 target case and different RIS sizes as well as number of pulses (see Table I). Therein, $\theta_1 = \theta_{RIS}^{R} = 30°$, $\phi_1 = \phi_{RIS}^{R} = 20°$, $\theta_2 = \theta_{RIS}^{T_a} = 0°$, $\phi_2 = \phi_{RIS}^{T_a} = 0°$, and in (a) $\mathrm{P}_{FA} = 10^{-4}$ while in (b) $\mathrm{P}_{FA} = 10^{-6}$.

APPENDIX

A. Evaluation Of The RIS-Induced Pattern

After some straightforward calculations, $\boldsymbol{\Sigma}$ can be expressed as

$$\boldsymbol{\Sigma} = \boldsymbol{\Gamma} \odot \boldsymbol{S}_1 \odot \boldsymbol{S}_2 = \boldsymbol{v}_1 \boldsymbol{v}_2^T, \tag{43}$$

with

$$\boldsymbol{v}_1 = [e^{-j2\pi \frac{(N-1)}{2} \Delta\kappa_u}, \ldots, e^{j2\pi \frac{(N-1)}{2} \Delta\kappa_u}]^T, \tag{44a}$$

$$\boldsymbol{v}_2 = [e^{-j2\pi \frac{(M-1)}{2} \Delta\kappa_v}, \ldots, e^{j2\pi \frac{(M-1)}{2} \Delta\kappa_v}]^T. \tag{44b}$$

As a consequence

$$|\mathbf{1}_N^T \, \boldsymbol{\Sigma} \, \mathbf{1}_M|^4 = |\mathbf{1}_N^T \boldsymbol{v}_1|^4 |\mathbf{1}_M^T \boldsymbol{v}_2|^4, \tag{45}$$

with

$$|\mathbf{1}_N^T \boldsymbol{v}_1|^4 = \left| \frac{\sin(\Delta\kappa_u \pi N)}{\sin(\Delta\kappa_u \pi)} \right|^4 \tag{46a}$$

and

$$|\mathbf{1}_M^T \boldsymbol{v}_1|^4 = \left| \frac{\sin(\Delta\kappa_v \pi M)}{\sin(\Delta\kappa_v \pi)} \right|^4. \tag{46b}$$

This article has been accepted for publication in IEEE Transactions on Vehicular Technology. This is the author's version which has not been fully edited and content may change prior to final publication. Citation information: DOI 10.1109/TVT.2021.3102315

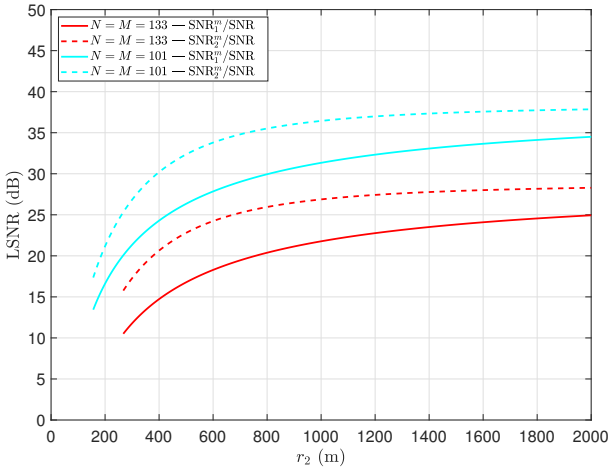

(a)

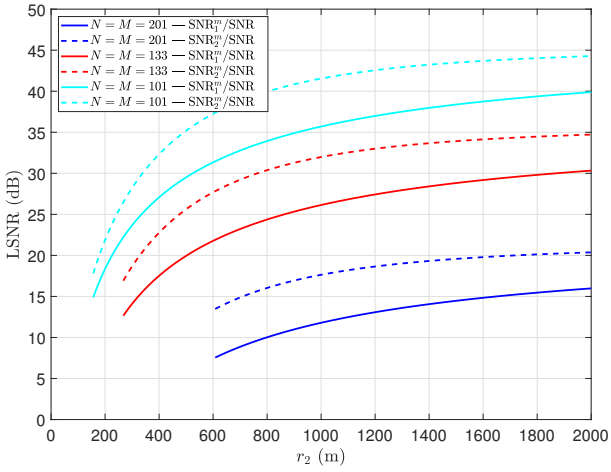

(b)

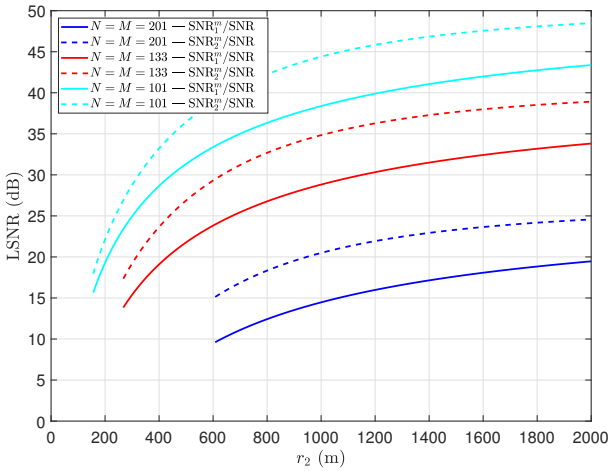

(c)

Fig. 12. LSNR versus r_2 assuming (a) $r_1 = 500$ m, (b) $r_1 = 750$ m, and (c) $r_1 = 1000$ m, different RIS sizes and parameters of Table I. In (a), the case $N = M = 301$ is not reported because for $r_1 = 500$ the RIS is no longer in the far-field region of the radar.

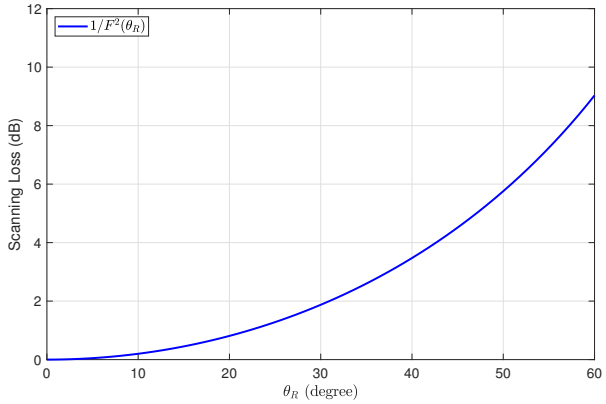

Fig. 13. Scanning Loss versus θ_R.

REFERENCES

[1] S. Hu, F. Rusek, and O. Edfors, "Beyond massive MIMO: The potential of data transmission with large intelligent surfaces," *IEEE Transactions on Signal Processing*, vol. 66, no. 10, pp. 2746–2758, May 2018.

[2] C. Liaskos, S. Nie, A. Tsioliaridou, A. Pitsillides, S. Ioannidis, and I. Akyildiz, "A new wireless communication paradigm through software-controlled metasurfaces," *IEEE Communications Magazine*, vol. 56, no. 9, pp. 162–169, Sep. 2018.

[3] E. Basar, M. Di Renzo, J. De Rosny, M. Debbah, M. Alouini, and R. Zhang, "Wireless communications through reconfigurable intelligent surfaces," *IEEE Access*, vol. 7, pp. 116753–116773, Aug. 2019.

[4] L. Yang, F. Meng, J. Zhang, M. O. Hasna, and M. D. Renzo, "On the performance of RIS-assisted dual-hop UAV communication systems," *IEEE Transactions on Vehicular Technology*, vol. 69, no. 9, pp. 10385–10390, Jun. 2020.

[5] W. Tang, M. Z. Chen, X. Chen, J. Y. Dai, Y. Han, M. Di Renzo, Y. Zeng, S. Jin, Q. Cheng, and T. J. Cui, "Wireless communications with reconfigurable intelligent surface: Path loss modeling and experimental measurement," *IEEE Transactions on Wireless Communications*, vol. 20, no. 1, pp. 421–439, Jan. 2021.

[6] S. Gopi, S. Kalyani, and L. Hanzo, "Intelligent reflecting surface assisted beam index-modulation for millimeter wave communication," *IEEE Transactions on Wireless Communications*, vol. 20, no. 2, pp. 983–996, Feb. 2021.

[7] W. Lu, B. Deng, Q. Fang, X. Wen, and S. Peng, "Intelligent reflecting surface-enhanced target detection in MIMO radar," *IEEE Sensors Letters*, vol. 5, no. 2, pp. 1–4, Feb. 2021.

[8] Y. U. Ozcan, O. Ozdemir, and G. Karabulut Kurt, "Reconfigurable intelligent surfaces for the connectivity of autonomous vehicles," *IEEE Transactions on Vehicular Technology*, pp. 1–1, Mar. 2021.

[9] W. Lu, Q. Lin, N. Song, Q. Fang, X. Hua, and B. Deng, "Target detection in intelligent reflecting surface aided distributed MIMO radar systems," *IEEE Sensors Letters*, pp. 1–1, Mar. 2021.

[10] Z. M. Jiang, M. Rihan, P. Zhang, L. Huang, Q. Deng, J. Zhang, and E. M. Mohamed, "Intelligent reflecting surface aided dual-function radar and communication system," *IEEE Systems Journal*, pp. 1–12, 2021.

[11] E. Calvanese Strinati, G. C. Alexandropoulos, V. Sciancalepore, M. Di Renzo, H. Wymeersch, D.-T. Phan-huy, M. Crozzoli, R. D'Errico, E. De Carvalho, P. Popovski, P. Di Lorenzo, L. Bastianelli, M. Belouar, J. E. Mascolo, G. Gradoni, S. Phang, G. Lerosey, and B. Denis, "Wireless environment as a service enabled by reconfigurable intelligent surfaces: The RISE-6G perspective," *arXiv preprint arXiv:2104.06265*, 2021.

[12] G. C. Alexandropoulos, N. Shlezinger, I. Alamzadeh, M. F. Imani, H. Zhang, and Y. C. Eldar, "Hybrid reconfigurable intelligent meta-surfaces: Enabling simultaneous tunable reflections and sensing for 6G wireless communications," *arXiv preprint arXiv:2104.04690*, 2021.

[13] R.S.P. Sankar, B. Deepak, and S. P. Chepuri, "Joint communication and radar sensing with reconfigurable intelligent surfaces," *arXiv preprint arXiv:2105.01966*, 2021.

[14] T. J. Cui, M. Q. Qi, X. Wan, J. Zhao, and Q. Cheng, "Coding metamaterials, digital metamaterials and programmable metamaterials," *Light: Science & Applications*, vol. 3, no. 10, pp. e218–e218, Oct. 2014.

[15] Q. Wu and R. Zhang, "Intelligent reflecting surface enhanced wireless network via joint active and passive beamforming," *IEEE Transactions on Wireless Communications*, vol. 18, no. 11, pp. 5394–5409, Nov. 2019.

[16] Q. Wu and R. Zhang, "Towards smart and reconfigurable environment: Intelligent reflecting surface aided wireless network," *IEEE Communications Magazine*, vol. 58, no. 1, pp. 106–112, Jan. 2020.

[17] M. Di Renzo, A. Zappone, M. Debbah, M. S. Alouini, C. Yuen, J. de Rosny, and S. Tretyakov, "Smart radio environments empowered by reconfigurable intelligent surfaces: How it works, state of research, and the road ahead," *IEEE Journal on Selected Areas in Communications*, vol. 38, no. 11, pp. 2450–2525, Nov. 2020.

[18] L. Subrt and P. Pechac, "Controlling propagation environments using intelligent walls," in *2012 6th European Conference on Antennas and Propagation (EUCAP)*, Mar. 2012, pp. 1–5.

[19] X. Tan, Z. Sun, J. M. Jornet, and D. Pados, "Increasing indoor spectrum sharing capacity using smart reflect-array," in *2016 IEEE International Conference on Communications (ICC)*, May 2016, pp. 1–6.

[20] O. Tsilipakos, A. C. Tasolamprou, A. Pitilakis, F. Liu, X. Wang, M. S. Mirmoosa, D. C. Tzarouchis, S. Abadal, H. Taghvaee, C. Liaskos, A. Tsioliaridou, J. Georgiou, A. Cabellos-Aparicio, E. Alarcón, S. Ioannidis, A. Pitsillides, I. F. Akyildiz, N. V. Kantartzis, E. N. Economou, C. M. Soukoulis, M. Kafesaki, and S. Tretyakov, "Toward intelligent metasurfaces: The progress from globally tunable metasurfaces to software-defined metasurfaces with an embedded network of controllers," *Advanced Optical Materials*, vol. 8, no. 17, pp. 2000783, Jul. 2020.

[21] Q. Wu, S. Zhang, B. Zheng, C. You, and R. Zhang, "Intelligent reflecting surface-aided wireless communications: A tutorial," *IEEE Transactions on Communications*, vol. 69, no. 5, pp. 3313–3351, May 2021.

[22] M. A. ElMossallamy, H. Zhang, L. Song, K. G. Seddik, Z. Han, and G. Y. Li, "Reconfigurable intelligent surfaces for wireless communications: Principles, challenges, and opportunities," *IEEE Transactions on Cognitive Communications and Networking*, vol. 6, no. 3, pp. 990–1002, Sep. 2020.

[23] L. Wei, C. Huang, G. C. Alexandropoulos, C. Yuen, Z. Zhang, and M. Debbah, "Channel estimation for RIS-empowered multi-user MISO wireless communications," *IEEE Transactions on Communications*, vol. 69, no. 6, pp. 4144–4157, Jun. 2021.

[24] C. Huang, Z. Yang, G. C. Alexandropoulos, K. Xiong, L. Wei, C. Yuen, and Z. Zhang, "Hybrid beamforming for RIS-empowered multi-hop terahertz communications: A DRL-based method," *2020 IEEE Globecom Workshops (GC Wkshps)*, pp. 1–6, Dec. 2020.

[25] C. Huang, Z. Yang, G. C. Alexandropoulos, K. Xiong, L. Wei, C. Yuen, Z. Zhang, and M. Debbah, "Multi-hop RIS-empowered terahertz communications: A DRL-based hybrid beamforming design," *IEEE Journal on Selected Areas in Communications*, vol. 39, no. 6, pp. 1663–1677, Jun. 2021.

[26] H. Wymeersch, J. He, B. Denis, A. Clemente, and M. Juntti, "Radio localization and mapping with reconfigurable intelligent surfaces: Challenges, opportunities, and research directions," *IEEE Vehicular Technology Magazine*, vol. 15, no. 4, pp. 52–61, Dec. 2020.

[27] H. Zhang, H. Zhang, B. Di, K. Bian, Z. Han, and L. Song, "Metalocalization: Reconfigurable intelligent surface aided multi-user wireless indoor localization," *IEEE Transactions on Wireless Communications*, pp. 1–1, 2021.

[28] A. M. Elzanaty, A. Guerra, F. Guidi, and M.-S. Alouini, "Reconfigurable intelligent surfaces for localization: Position and orientation error bounds," *arXiv preprint arXiv:2009.02818*, 2020.

[29] Z. Abu-Shaban, K. Keykhosravi, M. F. Keskin, G. C. Alexandropoulos, G. Seco-Granados, and H. Wymeersch, "Near-field localization with a reconfigurable intelligent surface acting as lens," *arXiv preprint arXiv:2010.05617*, 2020.

[30] A. Fascista, A. Coluccia, H. Wymeersch, and G. Seco-Granados, "RIS-aided joint localization and synchronization with a single-antenna mmwave receiver," *arXiv preprint arXiv:2010.14825*, 2020.

[31] C.-J. Wangy, S.-L. S., C.-K. Wen, and S. Jin, "Labeling multipath via reconfigurable intelligent surface," *arXiv preprint arXiv:2104.12062*, 2021.

[32] E. Björnson, H. Wymeersch, B. Matthiesen, P. Popovski, L. Sanguinetti, and E. De Carvalho, "Reconfigurable intelligent surfaces: A signal processing perspective with wireless applications," *arXiv preprint arXiv:2102.00742*, 2021.

[33] L. Zhao, Q. Cheng, X. K. Wang, M. J. Yuan, X. Zhou, X. J. Fu, M. Q. Qi, S. Liu, H. B. Chen, Y. Zhang, and T. J. Cui, "Controlling the bandwidth of terahertz low-scattering metasurfaces," *Advanced Optical Materials*, vol. 4, no. 11, pp. 1773–1779, Jul. 2016.

[34] L. H. Gao, Q. Cheng, J. Yang, S. J. Ma, J. Zhao, S. Liu, H. B. Chen, Q. He, W. X. Jiang, H. F. Ma, Q. Y. Wen, L. J. Liang, B. B. Jin, W. W. Liu, L. Zhou, J. Q. Yao, P. H. Wu, and T. J. Cui, "Broadband diffusion of terahertz waves by multi-bit coding metasurfaces," *Light: Science & Applications*, vol. 4, no. 9, pp. e324–e324, Sep. 2015.

[35] S. Buzzi, E. Grossi, M. Lops, and L. Venturino, "Radar target detection aided by reconfigurable intelligent surfaces," *IEEE Signal Processing Letters*, vol. 28, pp. 1315–1319, Jun. 2021.

[36] S. Buzzi, E. Grossi, M. Lops, and L. Venturino, "Foundations of MIMO radar detection aided by reconfigurable intelligent surfaces," *arXiv preprint arXiv:2105.09250*, 2021.

[37] A. Sume, M. Gustafsson, M. Herberthson, A. Janis, S. Nilsson, J. Rahm, and A. Orbom, "Radar detection of moving targets behind corners," *IEEE Transactions on Geoscience and Remote Sensing*, vol. 49, no. 6, pp. 2259–2267, Jun. 2011.

[38] O. Rabaste, E. Colin-Koeniguer, D. Poullin, A. Cheraly, J. F. Pétex, and H. K. Phan, "Around-the-corner radar: detection of a human being in non-line of sight," *IET Radar, Sonar & Navigation*, vol. 9, pp. 660–668(8), Jul. 2015.

[39] D. Tahmoush, J. Silvious, and B. Bender, "Radar surveillance in urban environments," in *2012 IEEE Radar Conference*, May 2012, pp. 0220–0225.

[40] K. Thai, O. Rabaste, J. Bosse, D. Poullin, I. D. H. Sáenz, T. Letertre, and T. Chonavel, "Detection–localization algorithms in the around-the-corner radar problem," *IEEE Transactions on Aerospace and Electronic Systems*, vol. 55, no. 6, pp. 2658–2673, Dec. 2019.

[41] D. Nüßler, A. Shoykhetbrod, S. Gütgemann, A. Küter, B. Welp, N. Pohl, and C. Krebs, "Detection of unmanned aerial vehicles (UAV) in urban environments," in *Emerging Imaging and Sensing Technologies for Security and Defence III; and Unmanned Sensors, Systems, and Countermeasures*, G. S. Buller, R. C. Hollins, R. A. Lamb, and M. Mueller, Eds. International Society for Optics and Photonics, Oct. 2018, vol. 10799, pp. 166 – 176, SPIE.

[42] X. Guo, C. S. Ng, E. de Jong, and A. B. Smits, "Concept of distributed radar system for mini-UAV detection in dense urban environment," in *2019 International Radar Conference (RADAR)*, Sep. 2019, pp. 1–4.

[43] M. I. Skolnik, *Radar Handbook*, New York, NY, USA: McGraw-Hill Education, 3rd edition, 2008.

[44] D. K. Barton, *Radar Equations for Modern Radar*, Artech House radar library. Norwood, MA, USA: Artech House, 2013.

[45] M. A. Richards, J. A. Scheer, and W. A. Holm, *Principles of Modern Radar: Basic principles*, Radar, Sonar & Navigation. Stevenage, UK: Institution of Engineering and Technology, 2010.

[46] L. Zhang, X. Q. Chen, S. Liu, Q. Zhang, J. Zhao, J. Y. Dai, G. D. Bai, X. Wan, Q. Cheng, G. Castaldi, V. Galdi, and T. J. Cui, "Space-time-coding digital metasurfaces," *Nature Communications*, vol. 9, no. 1, pp. 4334, Oct. 2018.

[47] C. Huang, A. Zappone, G. C. Alexandropoulos, M. Debbah, and C. Yuen, "Reconfigurable intelligent surfaces for energy efficiency in wireless communication," *IEEE Transactions on Wireless Communications*, vol. 18, no. 8, pp. 4157–4170, Aug. 2019.

[48] M. Di Renzo, M. Debbah, D. T. Phan-Huy, A. Zappone, M. S. Alouini, C. Yuen, V. Sciancalepore, G. C. Alexandropoulos, J. Hoydis, H. Gacanin, J. de Rosny, A. Bounceur, G. Lerosey, and M. Fink, "Smart radio environments empowered by reconfigurable ai meta-surfaces: an idea whose time has come," *EURASIP Journal on Wireless Communications and Networking*, vol. 2019, no. 1, pp. 129, May 2019.

[49] V. Arun and H. Balakrishnan, "Rfocus: Beamforming using thousands of passive antennas," in *17th USENIX Symposium on Networked Systems Design and Implementation (NSDI 20)*, Santa Clara, CA, Feb. 2020, pp. 1047–1061, USENIX Association.

[50] "NTT DOCOMO. (Jan. 2020). *DOCOMO Conducts World's First Successful Trial of Transparent Dynamic Metasurface.*," Website: https://www.nttdocomo.co.jp/english/info/media_center/pr/2020/0117_00.html, [Accessed: March 21, 2021].

[51] S. V. Hum and J. Perruisseau-Carrier, "Reconfigurable reflectarrays and array lenses for dynamic antenna beam control: A review," *IEEE Transactions on Antennas and Propagation*, vol. 62, no. 1, pp. 183–198, Jan. 2014.

[52] "Best readings in reconfigurable intelligent surfaces," Website: https://www.comsoc.org/publications/best-readings/reconfigurable-intelligent-surfaces, [Accessed: March 21, 2021].

[53] S. K. Chou, O. Yurduseven, H. Q. Ngo, and M. Matthaiou, "On the aperture efficiency of intelligent reflecting surfaces," *IEEE Wireless Communications Letters*, vol. 10, no. 3, pp. 599–603, Mar. 2021.

[54] R. J. Williams, E. de Carvalho, and T. L. Marzetta, "A communication model for large intelligent surfaces," in *2020 IEEE International*

Conference on Communications Workshops (ICC Workshops), Jun. 2020, pp. 1–6.

[55] Z. Wang, L. Tan, H. Yin, K. Wang, X. Pei, and D. Gesbert, "A received power model for reconfigurable intelligent surface and measurement-based validations," *arXiv preprint arXiv:2105.06082*, 2021.

[56] J. V. Di Franco and C. Kaiteris, "Radar performance review in clear and jamming environments," *IEEE Transactions on Aerospace and Electronic Systems*, vol. AES-17, no. 5, pp. 701–710, Sep. 1981.

[57] J. Marcum, "A statistical theory of target detection by pulsed radar," *IRE Transactions on Information Theory*, vol. 6, no. 2, pp. 59–267, Apr. 1960.

[58] H. L. Van Trees, *Optimum Array Processing: Part IV*, Detection, Estimation, and Modulation Theory. Hoboken, NJ, USA: Wiley, 2004.

[59] F. Nathanson, *Radar design principles: signal processing and the environment*, Mendham, NJ, USA: SciTech Pub, 1999.

[60] N. Levanon and E. Mozeson, *Radar signals*, Hoboken, NJ, USA: Wiley, 2004.

[61] A. Farina, *Antenna-based Signal Processing Techniques for Radar Systems*, Antennas and Propagation Library. Norwood, MA, USA: Artech House, 1992.

[62] C. W. Helstrom, *Statistical Theory of Signal Detection*, International Series of Monographs in Electronics and Instrumentation. New York, NY, USA: Pergamon, 2nd edition, 1968.

[63] A. Farina, A. De Maio, and S. Haykin, *The Impact of Cognition on Radar Technology*, Radar, Sonar & Navigation. Stevenage, UK: Institution of Engineering and Technology, 2017.

Augusto Aubry (M'12-SM'16) received the Dr. Eng. degree in telecommunication engineering (with honors) and the Ph.D. degree in electronic and telecommunication engineering both from the University of Naples Federico II, Naples, Italy, in 2007 and 2011, respectively. From February to April 2012, he was a Visiting Researcher with the Hong Kong Baptist University, Hong Kong. He is currently an assistant Professor with the University of Naples Federico II. His research interests include statistical signal processing and optimization theory, with emphasis on MIMO communications and radar signal processing. He is also the co-recipient of the 2013 Best Paper Award (entitled to B. Carlton) of the IEEE Transactions on Aerospace and Electronic Systems with the contribution "Knowledge-Aided (Potentially Cognitive) Transmit Signal and Receive Filter Design in Signal-Dependent Clutter".

Antonio De Maio (S'01-A'02-M'03-SM'07-F'13) received the Dr. Eng. (Hons.) and Ph.D. degrees in information engineering from the University of Naples Federico II, Naples, Italy, in 1998 and 2002, respectively. From October to December 2004, he was a Visiting Researcher with the U.S. Air Force Research Laboratory, Rome, NY, USA. From November to December 2007, he was a Visiting Researcher with the Chinese University of Hong Kong, Hong Kong. He is currently a Professor with the University of Naples Federico II. His research interest lies in the field of statistical signal processing, with emphasis on radar detection, optimization theory applied to radar signal processing, and multiple-access communications. He is the recipient of the 2010 IEEE Fred Nathanson Memorial Award as the young (less than 40 years of age) AESS Radar Engineer 2010 whose performance is particularly noteworthy as evidenced by contributions to the radar art over a period of several years, with the following citation for "robust CFAR detection, knowledge-based radar signal processing, and waveform design and diversity". He is the corecipient of the 2013 best paper award (entitled to B. Carlton) of the IEEE Transactions on Aerospace and Electronic Systems with the contribution "Knowledge-Aided (Potentially Cognitive) Transmit Signal and Receive Filter Design in Signal-Dependent Clutter".

Massimo Rosamilia (S'20) received the B.S. (with honors) and M.S. degrees in computer engineering from the University of Salerno, Fisciano, Italy, in 2017 and 2019, respectively. He is currently working toward the Ph.D. degree in information technologies and electrical engineering with the University of Naples Federico II, Naples, Italy. His research interest lies in the field of statistical signal processing, with emphasis on radar signal processing. He ranked second in the Student Contest of the 1st International Virtual School on Radar Signal Processing, in 2020, with the contribution "Simultaneous Radar Detection and Constrained Target Angle Estimation via Dinkelbach Algorithm".